Tensor-Network Analysis of Root Patterns in the XXX Model with Open Boundaries

Zhouzheng Ji^a, Pei Sun^{a,e,f}, Xiaotian Xu^{a,e,f1}, Yi Qiao^{a,e,f2}, Junpeng Cao^{b,c,d,e3} and Wen-Li Yang^{a,e,f}

^{a} Institute of Modern Physics, Northwest University, Xian 710127, China

^{b} Beijing National Laboratory for Condensed Matter Physics, Institute of Physics, Chinese Academy of Sciences, Beijing 100190, China

^{c} School of Physical Sciences, University of Chinese Academy of Sciences, Beijing 100049, China

^{d} Songshan Lake Materials Laboratory, Dongguan, Guangdong 523808, China

^{e} Peng Huanwu Center for Fundamental Theory, Xian 710127, China

^{f} Shaanxi Key Laboratory for Theoretical Physics Frontiers, Xian 710127, China

Abstract

The string hypothesis for Bethe roots represents a cornerstone in the study of quantum integrable systems, providing access to physical quantities such as the ground-state energy and the finite-temperature free energy. While the $t-W$ scheme and the inhomogeneous $T-Q$ relation have enabled significant methodological advances for systems with broken $U(1)$ symmetry, the underlying physics induced by symmetry breaking remains largely unexplored, due to the previously unknown distributions of the transfer-matrix roots. In this paper, we propose a new approach to determining the patterns of zero roots and Bethe roots for the $\Lambda - \theta$ and inhomogeneous Bethe ansatz equations using tensor-network algorithms. As an explicit example, we consider the isotropic Heisenberg spin chain with non-diagonal boundary conditions. The exact structures of both zero roots and Bethe roots are obtained in the ground state for large system sizes, up to ($N \simeq 60$ and 100). We find that even in the absence of $U(1)$ symmetry, the Bethe and zero roots still exhibit a highly structured pattern. The zero roots organize into bulk strings, boundary strings, and additional roots, forming two dominant lines with boundary-string attachments. Correspondingly, the Bethe roots can be classified into four distinct types: regular roots, line roots, arc roots, and paired-line roots. These structures are associated with a real-axis line, a vertical line, characteristic arcs in the complex plane, and boundary-induced conjugate pairs. Comparative analysis reveals that the $t-W$ scheme generates significantly simpler root topologies than those

---

^{1}Corresponding author: xtxu@nwu.edu.cn

^{2}Corresponding author: qiaoyi_joy@foxmail.com

^{3}Corresponding author: junpengcao@iphy.ac.cn

obtained via off-diagonal Bethe Ansatz. The developed framework not only resolves the root configuration problem in $U(1)$ symmetry-broken systems, but also provides a transferable approach for studying ground states, excitations, and finite-temperature properties in quantum integrable models.

Keywords: Bethe Ansatz; Tensor Network; Quantum Integrable Systems

1 Introduction

Quantum integrable systems provide a rigorous framework for the exact study of one-dimensional many-body problems. Since Bethe's solution of the spin-$\frac{1}{2}$ XXX chain [1], the Bethe Ansatz has remained a cornerstone of the field, yielding exact results for a broad class of integrable models [2, 3, 4]. For quantum integrable systems with boundary fields, integrability can be preserved within the quantum inverse scattering method (QISM) [6, 5], provided that the boundary reflections satisfy the boundary Yang–Baxter equations [7, 8, 9]. When the boundary fields are parallel, the Hamiltonian retains $U(1)$ symmetry and the Bethe Ansatz is well established [10, 11]. In contrast, generic non-diagonal boundary terms break the $U(1)$ symmetry yet the model remains integrable. To address this issue, several techniques have been developed, including gauge transformation [12], fusion-based $T - Q$ relation [13, 14], q-Onsager algebra [15, 16], separation of variables [17, 18], modified algebraic Bethe Ansatz [19, 20] and off-diagonal Bethe Ansatz [21, 22]. The eigenvalues of the transfer matrix of the quantum integrable systems without $U(1)$ symmetry are characterized by the inhomogeneous $T - Q$ relations. However, the associated Bethe Ansatz equations (BAEs) are inhomogeneous and the corresponding distributions of Bethe roots are very complicated. Consequently, the thermodynamic Bethe Ansatz [23, 24, 25] is no longer valid, and computing the exact physical properties in the thermodynamic limit becomes exceedingly difficult. Recently, based on off-diagonal Bethe Ansatz, the zero-root method (termed the $t - W$ scheme) has been proposed [26, 27], which effectively tackles the challenges posed by the inhomogeneous $T - Q$ relations. The key point is to analyze the zero roots of the transfer matrix, not those of the Q-operator (i.e., the Bethe roots).

The investigation of zero roots and Bethe roots is essential because their distribution patterns form the basis of the analysis of the thermodynamic limit and thermodynamic properties. Although the analytic structure of the inhomogeneous $T - Q$ relation and the $t - W$ relation are well understood, solving the associated constrained equations numerically remains challenging. Previous numerical studies of off-diagonal Bethe roots and zero roots have been restricted to small systems, typically $N \leq 12$, and served mainly to check theoretical conjectures [29, 30]. Particularly in high-rank quantum integrable models, the dimension of the local Hilbert space is large, and existing numerical approaches are insufficient for analyzing the structures of zero roots and Bethe roots. In contrast, tensor-network algorithms-

especially the density matrix renormalization group (DMRG) [31, 32, 33, 34, 35, 36], make it possible to obtain high-precision ground state and low-lying spectra for much larger systems, thereby building a practical bridge between functional formulas and numerical studies [37].

In this paper, we take the spin-1/2 XXX chain subject to arbitrary boundary fields as a benchmark to verify the efficacy and broad applicability of the numerical method developed herein. Within the QISM framework, we first represent the transfer matrix $t(u)$ as a matrix product operator (MPO) and compute its eigenvalue $\Lambda(u)$ for large lattice sizes using DMRG. The DMRG calculations were performed using the ITensor Library [38]. Then we solve the zeros of the transfer matrix from the numerically obtained $\Lambda(u)$ and verify them using the maximum modulus principle and the argument principle [39]; on this basis, we verify the correctness of the phase regions given in Ref. [40] and describe the concrete structural changes when parameters cross between these regions. Next, we solve the Bethe roots at large N directly from the inhomogeneous $T - Q$ relation, adapting the strategy outlined in Ref. [41], and summarize how their overall structural characteristics evolve with the boundary parameters, in particular the gradual restoration of $U(1)$ symmetry as the non-parallel boundary fields are reduced from finite values to zero.

The remainder of the paper is organized as follows: Sec. 2 introduces the model under consideration and its integrability, followed by a concise review of the ODBA formalism and the zero-root approach. Sec. 3 describes the DMRG/MPO implementation and the computation of $\Lambda(u)$; Sec. 4 presents zero roots together with their structural changes across parameter regions; Sec. 5 discusses the solution of Bethe roots and outlines their structural evolution; Sec. 6 concludes the work. Appendix A provides the MPO representation of the transfer matrix, while Appendix B presents the derivation of the maximum modulus principle. Appendices C and D provide validation data for the zero roots and the Bethe roots, respectively. Additionally, Appendix E illustrates the crossover behavior of the Bethe roots as the boundary parameters increase.

2 Integrability

Initially, let $\boldsymbol{V}$ be a two-dimensional linear space with an orthonormal basis $\{|m\rangle, m = 0, 1\}$. We adopt standard notations: for any matrix $A \in \text{End}(\boldsymbol{V})$, A_j denotes the embedding operator acting as A on the j-th space and as identity elsewhere in the tensor product $\boldsymbol{V}^{\otimes N}$. For $B \in \text{End}(\boldsymbol{V} \otimes \boldsymbol{V})$, B_{ij} acts nontrivially only on the i-th and j-th spaces.

We introduce the R-matrix $R_{0,j}(u) \in \mathrm{End}(\boldsymbol{V}_0 \otimes \boldsymbol{V}_j)$ as

$$R_{0,j}(u) = \begin{pmatrix} u+\eta & 0 & 0 & 0 \\ 0 & u & \eta & 0 \\ 0 & \eta & u & 0 \\ 0 & 0 & 0 & u+\eta \end{pmatrix}, \tag{2.1}$$

where u is the spectral parameter and η is the crossing parameter.

The R-matrix satisfies the following properties:

$$\begin{aligned} \text{Initial condition:} \quad & R_{0,j}(0) = \eta P_{0,j}, \\ \text{Unitarity:} \quad & R_{0,j}(u) R_{j,0}(-u) = \phi(u) \cdot \mathrm{id}, \\ \text{Crossing symmetry:} \quad & R_{0,j}(u) = -\sigma_0^y R_{0,j}^{t_0}(-u-\eta)\sigma_0^y, \\ \text{PT-symmetry:} \quad & R_{0,j}(u) = R_{j,0}(u) = R_{0,j}^{t_0 t_j}(u), \\ \mathbb{Z}_2\text{-symmetry:} \quad & \sigma_0^\alpha \sigma_j^\alpha R_{0,j}(u) = R_{0,j}(u)\sigma_0^\alpha \sigma_j^\alpha, \quad \alpha = x, y, z, \\ \text{Fusion condition:} \quad & R_{0,j}(\pm\eta) = \pm 2\eta P_{0,j}^{(\pm)}, \end{aligned} \tag{2.2}$$

where $\phi(u) = \eta^2 - u^2$, t_0 (t_j) denotes transposition in space $\boldsymbol{V}_0$ $(\boldsymbol{V}_j)$, and $P_{0,j}$ is the permutation operator.

The R-matrix satisfies the quantum Yang-Baxter equation (QYBE):

$$R_{1,2}(u_1 - u_2) R_{1,3}(u_1 - u_3) R_{2,3}(u_2 - u_3) = R_{2,3}(u_2 - u_3) R_{1,3}(u_1 - u_3) R_{1,2}(u_1 - u_2). \tag{2.3}$$

Define the monodromy matrices:

$$\begin{aligned} T_0(u) &= R_{0,N}(u - \theta_N) \cdots R_{0,1}(u - \theta_1), \\ \hat{T}_0(u) &= R_{1,0}(u + \theta_1) \cdots R_{N,0}(u + \theta_N), \end{aligned} \tag{2.4}$$

where $\boldsymbol{V}_0$ is the auxiliary space, $\boldsymbol{V}_1 \otimes \cdots \otimes \boldsymbol{V}_N$ is the quantum space, and $\{\theta_j\}$ are the inhomogeneity parameters.

The boundary reflection matrices are

$$K^-(u) = \begin{pmatrix} p+u & 0 \\ 0 & p-u \end{pmatrix}, \tag{2.5}$$

$$K^+(u) = \begin{pmatrix} q+u+\eta & \xi(u+\eta) \\ \xi(u+\eta) & q-u-\eta \end{pmatrix}, \tag{2.6}$$

where p, q, ξ are boundary parameters.

$K^-(u)$ satisfies the reflection equation

$$R_{1,2}(\lambda - u)\, K_1^-(\lambda)\, R_{2,1}(\lambda + u)\, K_2^-(u)$$
$$= \; K_2^-(u)\, R_{1,2}(\lambda + u)\, K_1^-(\lambda)\, R_{2,1}(\lambda - u). \tag{2.7}$$

and $K^+(u)$ satisfies the dual reflection equation

$$R_{1,2}(-\lambda + u)\, K_1^+(\lambda)\, R_{2,1}(-\lambda - u - 2\eta)\, K_2^+(u)$$
$$= \; K_2^+(u)\, R_{1,2}(-\lambda - u - 2\eta)\, K_1^+(\lambda)\, R_{2,1}(-\lambda + u). \tag{2.8}$$

Define the double-row monodromy matrix as

$$\boldsymbol{U}_0(u) = T_0(u) K_0^-(u) \hat{T}_0(u). \tag{2.9}$$

It satisfies the same reflection equation:

$$R_{1,2}(\lambda - u)\boldsymbol{U}_1(\lambda)R_{2,1}(\lambda + u)\boldsymbol{U}_2(u) = \boldsymbol{U}_2(u)R_{1,2}(\lambda + u)\boldsymbol{U}_1(\lambda)R_{2,1}(\lambda - u). \tag{2.10}$$

The transfer matrix is defined by

$$t(u) = \mathrm{tr}_0\{K_0^+(u)\boldsymbol{U}_0(u)\}. \tag{2.11}$$

In the tensor network representation, the transfer matrix $t(u)$ is illustrated in Fig. 1. It also satisfies the crossing symmetry

$$t(u) = t(-u - \eta). \tag{2.12}$$
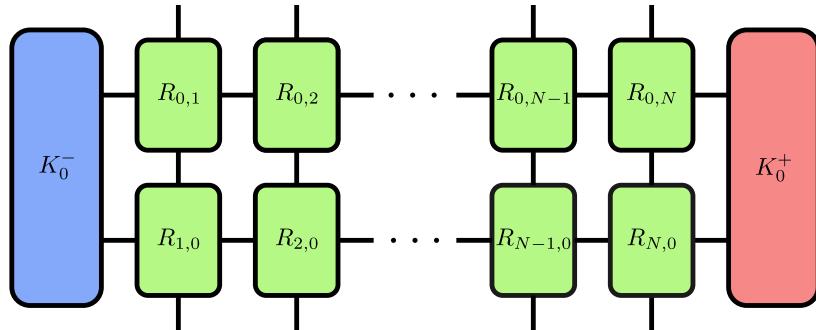
Figure 1: Tensor network diagram of the transfer matrix: horizontal bonds denote the auxiliary space labeled 0, and vertical bonds represent the quantum spaces labeled 1 through N.

From the QYBE and reflection equations, the transfer matrices commute:

$$[t(u), t(v)] = 0, \tag{2.13}$$

which guarantees the integrability of the system.

The Hamiltonian of the open XXX spin-$\frac{1}{2}$ chain with general boundary fields is

$$H = \sum_{n=1}^{N-1}(\sigma_n^x\sigma_{n+1}^x + \sigma_n^y\sigma_{n+1}^y + \sigma_n^z\sigma_{n+1}^z) + \frac{\eta}{p}\sigma_1^z + \frac{\eta}{q}(\sigma_N^z + \xi\sigma_N^x). \tag{2.14}$$

This Hamiltonian can be generated by the transfer matrix as

$$H = \eta \left.\frac{\partial \ln t(u)}{\partial u}\right|_{u=0,\{\theta_j=0\}} - N. \tag{2.15}$$

To ensure the Hermiticity of the Hamiltonian (2.14) for real η, the boundary parameters must satisfy:

$$q^* = q, \quad p^* = p, \quad \xi^* = \xi, \quad \text{when } \eta^* = \eta. \tag{2.16}$$

2.1   ODBA

Let us briefly review the ODBA method [22]. Using the properties of the R-matrix (2.2), the eigenvalue $\Lambda(u)$ of $t(u)$ satisfies:

$$\Lambda(u) = \Lambda(-u - \eta), \tag{2.17}$$

$$\Lambda(0) = a(0), \tag{2.18}$$

$$\Lambda(u) \sim 2u^{2N+2} + \dots, \quad u \to \pm\infty, \tag{2.19}$$

$$\Lambda(\theta_j)\Lambda(\theta_j - \eta) = a(\theta_j)d(\theta_j - \eta), \quad j = 1, \dots, N, \tag{2.20}$$

where $a(u)$ and $d(u)$ are defined as

$$a(u) = \frac{2u + 2\eta}{2u + \eta}(u + p)[(1 + \xi^2)^{\frac{1}{2}}u + q]\prod_{j=1}^{N}(u + \theta_j + \eta)(u - \theta_j + \eta),$$
$$d(u) = a(-u - \eta). \tag{2.21}$$

These conditions allow us to construct the following inhomogeneous $T - Q$ relation for each eigenvalue $\Lambda(u)$:

$$\Lambda(u) = a(u)\frac{Q(u - \eta)}{Q(u)} + d(u)\frac{Q(u + \eta)}{Q(u)} + 2[1 - (1 + \xi^2)^{\frac{1}{2}}]u(u + \eta)$$

$$\times \frac{\prod_{j=1}^{N}(u+\theta_j)(u-\theta_j)(u+\theta_j+\eta)(u-\theta_j+\eta)}{Q(u)}. \tag{2.22}$$

The function $Q(u)$ is parameterized by N Bethe roots $\{\lambda_j \mid j = 1, \ldots, N\}$ as follows:

$$Q(u) = \prod_{j=1}^{N}(u-\lambda_j)(u+\lambda_j+\eta). \tag{2.23}$$

Now we can take the homogeneous limit $\theta_j \to 0$. In this case, the functional $T - Q$ relation is

$$\begin{aligned}
\Lambda(u) = {} & \frac{2(u+\eta)^{2N+1}}{2u+\eta}(u+p)[(1+\xi^2)^{\frac{1}{2}}u+q]\frac{Q(u-\eta)}{Q(u)} \\
& + \frac{2u^{2N+1}}{2u+\eta}(u-p+\eta)[(1+\xi^2)^{\frac{1}{2}}(u+\eta)-q]\frac{Q(u+\eta)}{Q(u)} \\
& + 2[1-(1+\xi^2)^{\frac{1}{2}}]\frac{[u(u+\eta)]^{2N+1}}{Q(u)},
\end{aligned} \tag{2.24}$$

and the BAEs read

$$\begin{aligned}
(\frac{\lambda_j+\eta}{\lambda_j})^{2N+1}\frac{(\lambda_j+p)[(1+\xi^2)^{\frac{1}{2}}\lambda_j+q]}{(\lambda_j-p+\eta)[(1+\xi^2)^{\frac{1}{2}}(\lambda_j+\eta)-q]} = {} & -\frac{Q(\lambda_j+\eta)}{Q(\lambda_j-\eta)} \\
& - \frac{[1-(1+\xi^2)^{\frac{1}{2}}](2\lambda_j+\eta)(\lambda_j+\eta)^{2N+1}}{(\lambda_j-p+\eta)[(1+\xi^2)^{\frac{1}{2}}(\lambda_j+\eta)-q]Q(\lambda_j-\eta)}, \quad j = 1, \ldots, N.
\end{aligned} \tag{2.25}$$

The eigenvalue of the Hamiltonian in (2.14) is given by

$$E = \sum_{j=1}^{N}\frac{2\eta^2}{\lambda_j(\lambda_j+\eta)} + \frac{\eta}{p} + \frac{\eta\sqrt{1+\xi^2}}{q} + N - 1. \tag{2.26}$$

2.2 Zero-root method

Now, let us recall the zero-root method [26, 27]. Using (2.17) and (2.19), together with the fact that $\Lambda(u)$ is a degree-$(2N + 2)$ polynomial, we can simply parameterize it by its zero roots $\{z_j \mid j = 1, \ldots, N+1\}$ as

$$\Lambda(u) = 2\prod_{j=1}^{N+1}(u-z_j)(u+z_j+\eta). \tag{2.27}$$

Thus, the constrained equations (2.18) and (2.20) become

$$\prod_{j=1}^{N+1}(-z_j)(z_j+\eta) = a(0), \tag{2.28}$$

and

$$\prod_{j=1}^{N+1}(\theta_j - z_j)(\theta_j + z_j + \eta) = a(\theta_j)a(-\theta_j), \quad j = 1,\ldots,N. \tag{2.29}$$

In the homogeneous limit $\{\theta_j = 0 \mid j = 1,\ldots,N\}$, Eq. (2.28) and (2.29) becomes

$$\prod_{j=1}^{N+1}(-z_j)(z_j + \eta) = 2pq, \tag{2.30}$$

and

$$\left.\big[\Lambda(u)\Lambda(u - \eta)\big]^{(n)}\right|_{u=0} = \left.\big[a(u)a(-u)\big]^{(n)}\right|_{u=0}, \qquad n = 0, 1, \ldots, N-1, \tag{2.31}$$

where the superscript (n) denotes the n-th derivative with respect to u.

The eigenvalue of the Hamiltonian (2.14) can be expressed in terms of the zero roots $\{z_j\}$ as follows:

$$E = -\sum_{j=1}^{N+1}\frac{\eta^2}{z_j(z_j + \eta)} - N. \tag{2.32}$$

3 DMRG

The density-matrix renormalization group (DMRG) method was originally a high-precision numerical algorithm for investigating the ground state and low-lying excitations of low-dimensional, strongly-correlated quantum many-body systems. Later, a variety of techniques were developed that extended DMRG from zero temperature to finite temperatures and from the calculation of static quantities to the evaluation of time-dependent or dynamical correlation functions [42]. These advances not only broadened the scope of DMRG but also stimulated the emergence of a new generation of algorithms based on so-called tensor-network states, which represent a quantum state as a product of interconnected tensors and provide a new tool for exploring quantum many-body systems.

First, let us explain how DMRG obtains the ground state in the language of tensor networks. Consider a Hermitian Hamiltonian H acting on a vector space formed by the tensor product of N local spaces, each of dimension d. We depict H as a tensor in Fig. 2.

The DMRG method approximates the ground state of H by constructing a Matrix Product State (MPS) representation, which is a tensor network that captures the entanglement structure of the system. Starting from an initial MPS, the algorithm performs n sweeps of energy-minimizing optimization: at each step it updates one or two site tensors and

Figure 2: Tensor network representation of the Hamiltonian H. The network has N input and N output indices, each corresponding to a local Hilbert space of dimension d.

applies a singular-value decomposition (SVD), truncating the singular values according to two criteria—a maximum bond dimension D and a maximum allowed truncation error that limits the discarded weight. After n sweeps, this variational procedure yields an MPS whose accuracy is controlled jointly by the bond-dimension limit D, the truncation-error threshold, and the total number of sweeps. In our calculations, the truncation error is set to 1×10^{-12}, the maximum bond dimension is $D = 200$, and the convergence criterion is defined by a minimum of 30 sweeps with an energy convergence tolerance of 1×10^{-14}. The overall goal of the DMRG procedure is illustrated schematically in Fig. 3.

Figure 3: Here $E_0 (\leq E_1 \leq E_2 \dots)$ denotes the lowest variational energy obtained by DMRG, which approximates the true ground-state eigenvalue of H. The shaded region below H indicates the MPS representation of the approximate ground state corresponding to this energy.

To make the algorithm efficient, the Hamiltonian H is usually encoded in the form of a Matrix Product Operator (MPO); see Fig. 4. This MPO representation proves particularly advantageous for numerical implementations, including tensor network contractions.

$$H = \text{[MPO tensor network diagram]}$$

Figure 4: Tensor network representation of the Hamiltonian H in MPO form. Each tensor represents a local operator with one physical index on the top and bottom, and virtual indices connecting neighboring sites.

Meanwhile, Fig.1 illustrates that the transfer matrix $t(u)$ can be expressed as a tensor network in MPO form. The transformation from the double-row transfer matrix to the MPO form is illustrated in Fig. 5. The derivation details are provided in Appendix A.

Consequently, the transfer matrix is reformulated as an MPO that can be directly handled by standard tensor-network techniques.
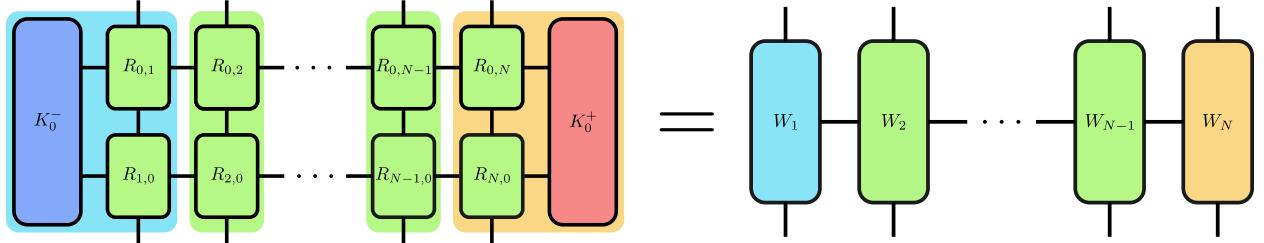
Figure 5: Transformation of the double-row transfer matrix into an MPO. Each local tensor W_i on the right is obtained by contracting the vertical pair of R-matrices at site i in the double-row structure, along with the adjacent boundary tensors at the first and last sites.

It should be noted that, although the Hamiltonian and the transfer matrix commute, their respective ground states are not identical. Our goal is to compute the eigenvalues of the transfer matrix within the ground state of the Hamiltonian given in Eq. (2.14). Therefore, we first need to obtain the ground state of the Hamiltonian. To address this, we employ the ITensor library [38]. Within ITensor, the MPO representation of the Hamiltonian can be constructed straightforwardly, and its ground state MPS can be efficiently obtained through DMRG. Subsequently, we compute the inner product of the Hamiltonian's ground state MPS with the transfer-matrix MPO, thereby extracting the eigenvalues of the latter.

The errors stem from two sources: first, the numerical error introduced by DMRG in computing $\Lambda(u)$; second, the additional error incurred when extracting the zeros or Bethe roots from the DMRG-supplied $\Lambda(u)$. Using the $U(1)$-symmetric case as a benchmark, we confirm that both contributions are extremely small; in the $U(1)$-symmetry-broken case, a dedicated verification routine further confirms that the second error remains negligible.

4   Zero roots

Using the approach described in the previous section, the eigenvalue $\Lambda(u)$ of the transfer matrix $t(u)$ at any u can be readily computed within the ground state of the Hamiltonian Eq. (2.14), even for large N. We can use the DMRG-computed $\Lambda(u)$ to locate its zeros. The Bethe Ansatz-DMRG (BA-DMRG) procedure is summarized as follows:

1. Obtain the ground state MPS of the Hamiltonian.

2. Represent the transfer matrix $t(u)$ as an MPO.

3. Select a set of interpolation points $\{u_j\}$ and compute the corresponding eigenvalues $\Lambda(u_j)$ of the transfer matrix in the ground state.

4. Reconstruct $\Lambda(u)$ using the Lagrange interpolation method.

5. Determine the zero roots of $\Lambda(u)$ through numerical root-finding algorithms.

6. Verify the correctness of the obtained roots (the specific procedures and principles will be presented in the following sections); if the verification fails, return to step 3 and use the current results as new interpolation points.

In step 3, from Eq. (2.27), the eigenvalue polynomial $\Lambda(u)$ can be parameterized in terms of $2N + 2$ points $\{z_j, -z_j - \eta \mid j = 1, \ldots, N + 1\}$. To improve the precision of the interpolation procedure, the interpolation nodes $\{u_j\}_{j=1}^{2N+2}$ are constructed as $\{x_j, -x_j - \eta \mid j = 1, \ldots, N + 1\}$. Instead, they are designed based on the specific structural properties of the zero roots. In particular, the nodes are chosen as $x_j = \frac{\eta}{2} + \frac{i}{N}\left(j - \frac{N}{2}\right)^k$, where $j = 1, 2, \ldots, N$ and $k \in [1, 1.1]$ (where i denotes the imaginary unit). This choice ensures a denser sampling near the accumulation region of the roots, thereby enhancing the accuracy of the interpolation.

In step 4, through a Lagrange polynomial representation, any degree-$(2N+2)$ polynomial can be uniquely determined by its values at $2N+3$ arbitrary grid points. In the present case (see Eq. (2.27)), since the leading coefficient of $\Lambda(u)$ is known to be 2, only $2N + 2$ points are required to fully specify the polynomial

$$\Lambda(u) = 2 \prod_{j=1}^{2N+2} (u - u_j) + \sum_{j=1}^{2N+2} \Lambda(u_j) \prod_{\substack{1 \leq k \leq 2N+2 \\ k \neq j}} \frac{u - u_k}{u_j - u_k}, \tag{4.1}$$

where the interpolation nodes $\{u_j\}_{j=1}^{2N+2}$ are those defined in step 3.

In step 6, if the root verification fails, the current results are used as updated interpolation nodes, and the zero roots are recalculated iteratively until the desired precision is achieved.

4.1 Ground state solution with U(1) symmetry

At $\xi = 0$, the two boundary fields are parallel, endowing the system with a global $U(1)$ symmetry. Consequently, the BAEs in Eq. (2.25) reduce to the following homogeneous form:

$$(\frac{\lambda_j + \eta}{\lambda_j})^{2N+1}\frac{(\lambda_j + p)(\lambda_j + q)}{(\lambda_j + \eta - p)(\lambda_j + \eta - q)} = -\frac{Q(\lambda_j + \eta)}{Q(\lambda_j - \eta)}, \quad j = 1, \ldots, N. \tag{4.2}$$

In this case, the inhomogeneous term in the $T - Q$ relation vanishes and part of the N Bethe roots may take the value of infinity. The function $Q(u)$ is thus reduced to

$$Q(u) = \prod_{j=1}^{M}(u - \lambda_j)(u + \lambda_j + \eta), \qquad M = 0, \ldots, N. \tag{4.3}$$

For the homogeneous BAEs (4.2), we recast them into logarithmic form to enhance numerical accuracy. This well-established method is used here to generate reference data for comparison with the BA-DMRG solution, thereby verifying the reliability of the latter.

For convenience, we put $\eta = 1$, $\mu_j = i\lambda_j - \frac{1}{2}$, $\hat{p} = p - \frac{1}{2}$, $\hat{q} = q - \frac{1}{2}$. Eq. (4.2) can be rewritten as

$$\frac{(\mu_j - i\hat{q})(\mu_j - i\hat{p})}{(\mu_j + i\hat{q})(\mu_j + i\hat{p})} \left(\frac{\mu_j - \frac{i}{2}}{\mu_j + \frac{i}{2}}\right)^{2N} = \prod_{\substack{l=1 \\ l \neq j}}^{M} \frac{(\mu_j - \mu_l - i)(\mu_j + \mu_l - i)}{(\mu_j - \mu_l + i)(\mu_j + \mu_l + i)}. \tag{4.4}$$

Taking the logarithm of Eq. (4.4), we have

$$\theta_{2\hat{p}}(\mu_j) + \theta_{2\hat{q}}(\mu_j) + 2N\theta_1(\mu_j) = 2\pi I_j + \sum_{l=1}^{M}[\theta_2(\mu_j - \mu_l) + \theta_2(\mu_j + \mu_l)] - \theta_1(\mu_j), \tag{4.5}$$

where $\theta_n(x) = 2\arctan(2x/n)$, and $\{I_j\}$ are certain integers (half-odd integers) for $N - M$ odd ($N - M$ even).

Through analytical considerations [22], it can be concluded that, for the ground state, the ratio $\frac{M}{N} = \frac{1}{2}$ holds, and the quantum numbers $\{I_j\}$ are continuously distributed. For even N, the quantum numbers can be expressed as $I_j = -\frac{M}{2} + j - 1$, where $j = 1, 2, \ldots, M$. By substituting these quantum numbers into Eq. (4.5), the M Bethe roots $\{\mu_j\}$ corresponding to the ground state can be numerically determined. After transforming $\{\mu_j\}$ into $\{\lambda_j\}$, $Q(u)$ can be constructed, from which $\Lambda(u)$ is obtained via Eq. (2.24). Finally, the zero roots $\{z_j\}$ are extracted using a standard numerical root-finding procedure.

Fig. 6 compares the zero roots obtained from the logarithmic BAEs, which are solved with high numerical precision, and those computed using the BA-DMRG method, showing

(a) Global configuration of zero roots **(b)** Enlarged view of the right cluster
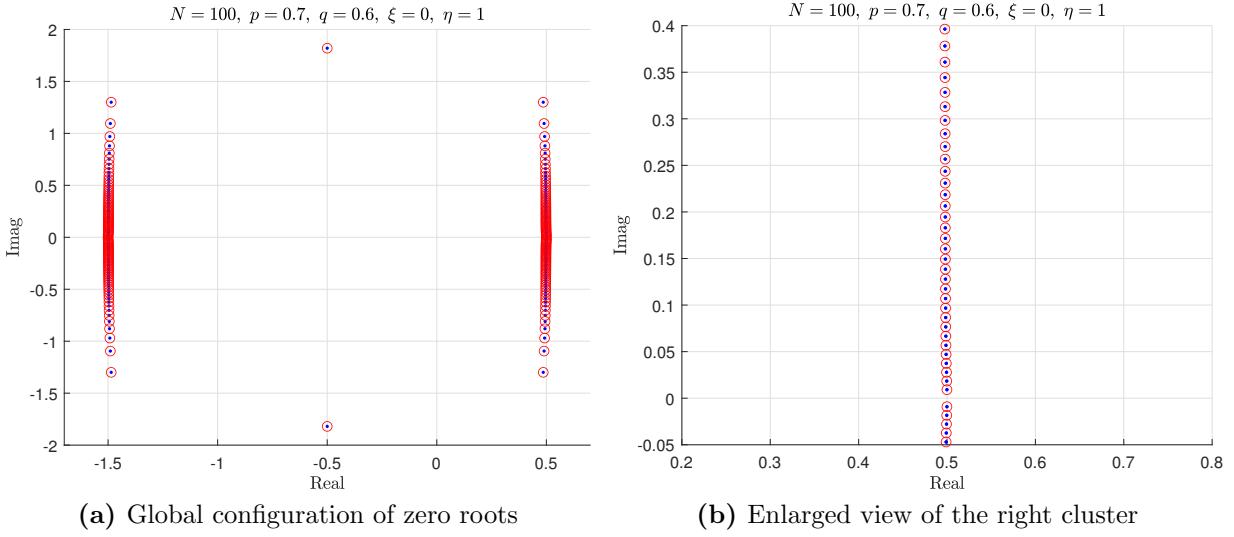
Figure 6: Distribution of zero roots in the complex plane with parameters $N = 100$, $p = 0.7$, $q = 0.6$, $\xi = 0$, and $\eta = 1$. Red circles represent zero roots obtained from the logarithmic form of the BAEs, and blue dots correspond to those computed using the BA-DMRG method. Subplot (b) is an enlarged view of the central portion of the right-hand line in subplot (a).

an almost perfect match. Since the BAEs solutions are taken as the accurate benchmark, the strong agreement between the two sets of results—with the maximum absolute error of 6.72×10^{-8}—demonstrates that the BA-DMRG method can reliably and accurately compute the zero roots.

4.2 Ground state solution without U(1) symmetry

At $\xi \neq 0$, the two boundary fields are non-parallel, so the system no longer possesses global $U(1)$ symmetry. The BAEs in Eq. (2.25) are inhomogeneous, so their logarithmic form is unavailable. Nevertheless, we can still compute the zero roots with the BA-DMRG method. The results are presented in Fig. 7, while the detailed numerical values of the roots and the auxiliary data are provided in Table C.1.

For large N, $\Lambda(u)$ is of high degree, and a poor choice of interpolation nodes can stall convergence. In the homogeneous case, we have verified that $\Lambda(u)$ of the transfer matrix obtained via DMRG is highly accurate (the relative error of $\Lambda(u)$ at $N = 100$ computed by DMRG is no worse than 10^{-10}). Based on this, it suffices to verify the accuracy of the iteration procedure. Consequently, the zero roots obtained by BA-DMRG demand an
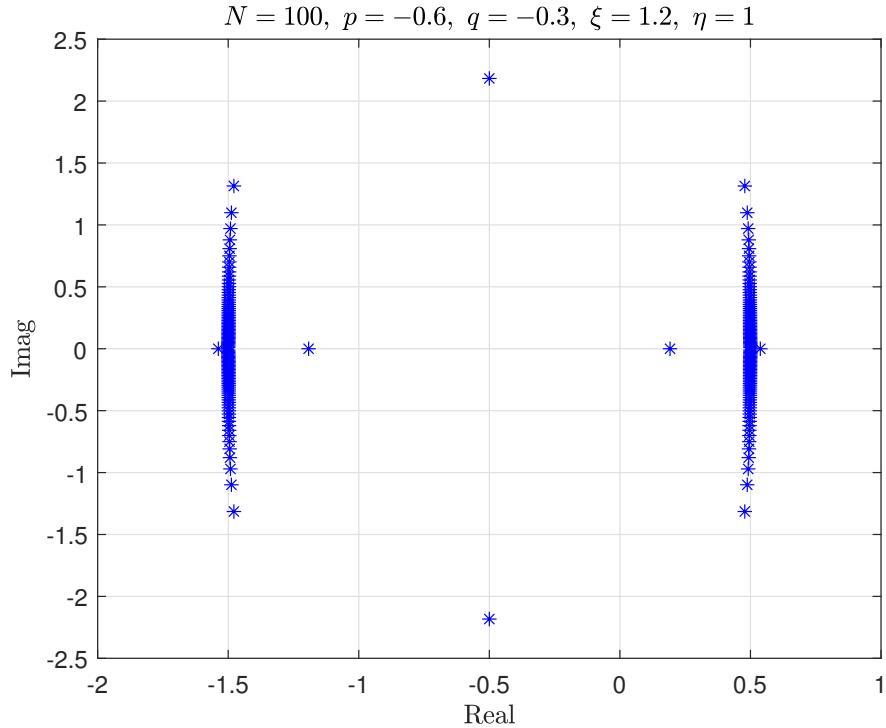
Figure 7: Distribution of zero roots in the complex plane with parameters $N = 100$, $p = -0.6$, $q = -0.3$, $\xi = 1.2$, and $\eta = 1$.

independent accuracy check. At large lattice sizes even sizeable displacements of some roots may leave the energy practically unchanged, so validation via the energy expression (2.32) is no longer sufficiently stringent. To test the reliability of the zero roots provided by BA-DMRG method, we therefore employ two independent tools: the maximum-modulus principle and the argument principle. The former exploits the local analytic properties of the function $\Lambda(u)$, whereas the latter directly counts the numbers of zeros and poles inside a closed contour.

4.2.1 Maximum modulus principle

Let $\{z_j\}$ denote the computed zero roots, for which $\Lambda(z_j)$ should ideally vanish. Owing to the high degree of $\Lambda(u)$ for large system size N, the evaluated $\Lambda(z_j)$ may appear large, so $\{z_j\}$ might seem not to be true zeros. In reality, the genuine zeros of $\Lambda(u)$ lie extremely close to the computed $\{z_j\}$; in other words, $\{z_j\}$ are in fact highly accurate. This can be rigorously justified using the maximum modulus principle. The maximum modulus principle is a fundamental result in complex analysis. It states that:

If a function is analytic and non-constant within a domain, then its maximum modulus

cannot occur strictly inside the domain–it must occur only on the boundary.

This property places strong constraints on the behavior of analytic functions in the complex plane. Based on this principle, we consider a useful corollary:

Suppose a function $f(z)$ is analytic on the closed disk $|z| \leq R$, and there exists a constant $a > 0$ such that

$$|f(z)| > a \quad \textit{for all } |z| = R, \quad \textit{and} \quad |f(0)| < a, \tag{4.6}$$

then $f(z)$ must have at least one zero in the open disk $|z| < R$.

The derivation of the corollary is given in Appendix B. More generally, if the modulus $|f(z)|$ demonstrates concave behavior around a point z_0, then $f(z)$ must vanish at some point within the enclosed region. This reflects the fact that analytic functions cannot exhibit a strict local minimum of modulus unless the function is identically zero or vanishes somewhere inside the domain.

We apply this result to the eigenvalue function $\Lambda(u)$ obtained from the DMRG calculations. For each candidate zero root z_j, we numerically evaluate the modulus $|\Lambda(u)|$ over a neighborhood around z_j in the complex plane. In all tested cases, the modulus $|\Lambda(u)|$ exhibits a clear valley-shaped behavior: its value at z_j is significantly smaller than that on the surrounding contour. According to the corollary of the maximum-modulus principle, such a valley-shaped behavior guarantees the existence of a true zero within the neighborhood. Fig. 8 shows $|\Lambda(u)|$ sampled around three representative zero-root candidates listed in Table C.1: $z_1 = -1.537797484404868 + 0.000000000000011i$, $z_{101} = -0.500000001273242 + 2.182890275358742i$, and $z_{37} = -1.498541855014614 + 0.190968750516886i$. These three points represent the typical structural types of zero roots in the system. The $|\Lambda(u)|$ computed by DMRG exhibits a pronounced concave dip, thereby confirming the reliability of the identified zero-root candidates.

The maximum modulus principle allows for a visually intuitive identification of zeros via the concave behavior of the modulus. It provides direct and accessible evidence of zero-root locations. This approach is particularly effective when the evaluation points lie along straight lines, where plotting is efficient. However, verifying zeros across the full complex plane becomes computationally expensive if high visual resolution is required. Therefore, to rigorously validate all candidate points, we further employ the argument principle, which gives a definitive count of zeros within closed contours.
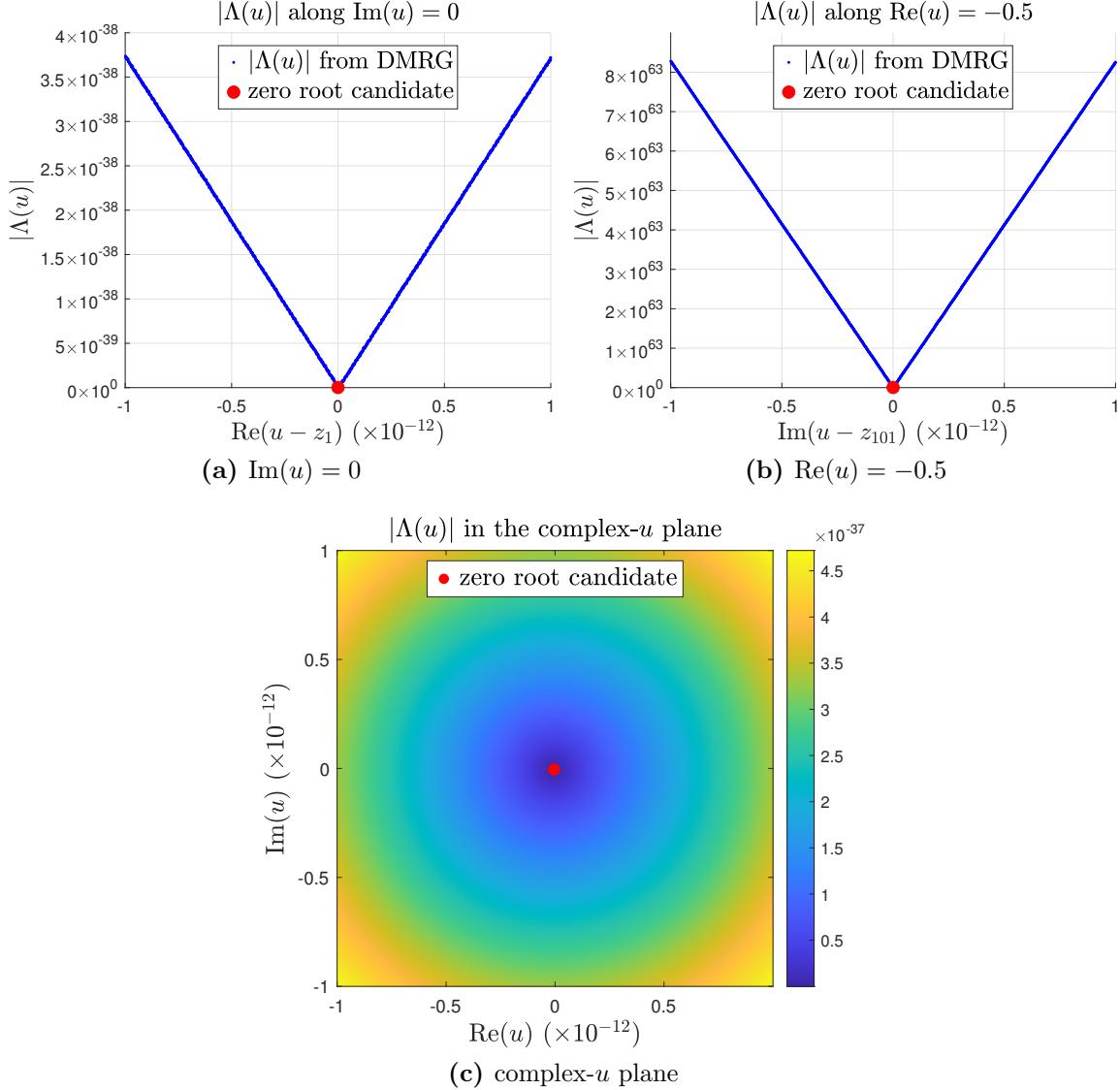
Figure 8: Local behavior of the eigenvalue modulus $|\Lambda(u)|$ around three representative zero-root candidates (indices 1, 101, and 37 in Table C.1), with $z_1 = -1.537797484404868 + 0.000000000000011i$, $z_{101} = -0.50000001273242 + 2.182890275358742i$, and $z_{37} = -1.498541855014614 + 0.190968750516886i$. All panels are plotted in relative coordinates centered at the respective zero-root candidates. (a) $|\Lambda(u)|$ along the real axis ($\mathrm{Im}(u) = 0$). (b) $|\Lambda(u)|$ along the vertical line $\mathrm{Re}(u) = -0.5$. (c) Two-dimensional modulus distribution of $|\Lambda(u)|$ in the complex-u plane obtained by DMRG. A uniform coordinate precision of 10^{-12} is used throughout.

4.2.2 Argument principle

The argument principle establishes a fundamental connection between the number of zeros and poles of a meromorphic function inside a closed contour and the total change in the function's argument along that contour:

$$N_{\text{zeros}} - N_{\text{poles}} = \frac{1}{2\pi i} \oint_C \frac{f'(z)}{f(z)} \, dz = \frac{1}{2\pi} \Delta_C \arg f(z), \tag{4.7}$$

where $\Delta_C \arg f(z)$ denotes the net change in the function's argument as the contour C is traversed once in the positive (counterclockwise) direction.

In this work, the eigenvalue function $\Lambda(u)$ is analytic and free of poles. Hence, the total argument change along any closed contour directly equals the number of enclosed zeros.

To apply this principle numerically, we construct a small discrete closed contour around each candidate zero root u_0, composed of five evaluation points arranged as shown in Fig. 9. These points are symmetrically offset from u_0 by a small value δ along the real and imaginary directions and connected in a counterclockwise order to form a rectangular loop. The path starts and ends at the same point to ensure formal closure. Importantly, the parameter δ is chosen to be much smaller than the minimal distance between any two zero roots. This guarantees that each contour encloses at most one zero. With this contour, $\Delta_C \arg f(z) = \arg f(u_5) - \arg f(u_1)$.
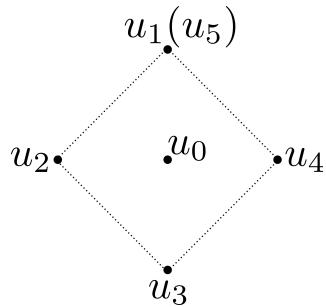
Figure 9: Illustration of the discrete rectangular contour used in the argument principle test. The path is centered at the candidate root u_0 and consists of five points: $u_1 = u_0 + i\delta$, $u_2 = u_0 - \delta$, $u_3 = u_0 - i\delta$, $u_4 = u_0 + \delta$, and $u_5 = u_1$ to close the loop. The points are symmetrically offset by a small value δ along the real and imaginary directions. This minimal closed contour enables phase unwrapping to detect whether exactly one zero lies inside.

The rationale for using these five points lies in the nature of argument evaluation: when computing $\arg f(z)$ numerically, the returned values lie within the principal branch $(-\pi, \pi]$.

As such, the raw argument at the starting arg $f(u_1)$ and ending points arg $f(u_5)$ is always the same, even if the functions phase has changed by a multiple of 2π along the path. To detect any such hidden change, intermediate points are needed. These enable the use of phase unwrapping, a technique that corrects artificial phase jumps by adding or subtracting 2π whenever adjacent phase differences exceed π.

With this setup, if the path encloses a zero, the unwrapped argument will exhibit a net change close to 2π, consistent with the theoretical prediction. Conversely, if no zero is enclosed, the total unwrapped change remains zero. This makes the verification result (4.7) strictly binary–either 0 or 1.

Table 1 illustrates this approach using the candidate zero root indexed 202 in Table C.1, showing how the unwrapped total argument change depends on the choice of δ and confirming the detection of a single zero. The zero is successfully detected when $\delta = 10^{-14}$, but it is missed as δ is reduced to 10^{-15}, indicating that $z_{202} = 0.537797484404868 - 0.00000000000$ $0011i$ is located with an accuracy of the order of 10^{-14}. All candidate roots obtained by the BA-DMRG method and their verifications are summarized in Table C.1. For the 202 zero roots at $N = 100$, the accuracy is better than 1×10^{-12}, providing strong numerical evidence for the correctness of the roots.

Table 1: Effect of the unwrapping threshold δ on the net argument change and the resulting zero count $\Delta = \frac{1}{2\pi}\Delta_C \arg f(z)$. The five sampling points $u_1, \ldots, u_5$ (locations as shown in Fig. 9) encircle the candidate root $z_{202} = 0.537797484404868 - 0.000000000000011i$. With $\arg_j \equiv \arg f(u_j)$, the unwrapped $\arg_j$ are listed for each δ; values in parentheses give the raw principal values.

δ	$\arg_1$	$\arg_2$	$\arg_3$	$\arg_4$	$\arg_5$	Δ
10^{-13}	1.557 (1.557)	3.142 (-3.142)	4.726 (-1.557)	6.283 (0)	7.84 (1.557)	1.0
10^{-14}	1.436 (1.436)	3.142 (-3.142)	4.847 (-1.436)	6.283 (0)	7.719 (1.436)	1.0
10^{-15}	0.634 (0.634)	0 (0)	-0.634 (-0.634)	0 (0)	0.634 (0.634)	0.0

This approach achieves high efficiency by evaluating the function at only a few strategically chosen points per candidate. It eliminates the need for dense sampling, making it particularly advantageous for large-scale zero detection tasks that demand rigorous numerical accuracy. We note that the dominant source of error is the numerical inaccuracy introduced by DMRG when computing $\Lambda(u)$.

4.3 Structure of the zero roots

After confirming the accuracy of the zero roots, we proceed to analyze their structural properties as functions of the boundary parameters. The phase diagram and accompanying description of root structures, first presented in Ref. [40], are recast into the notation used here in Fig. 10 and Table 2. For convenience, we define $\bar{q} = \frac{q}{\sqrt{1+\xi^2}}$. While these structural characteristics have been extensively studied in Ref. [40], the corresponding phase diagram for the off-diagonal case was established using a relatively small system size ($N \sim 10$). In this work, we verify these conclusions for large system size ($N \sim 100$) using the BA-DMRG method. Furthermore, we provide a detailed analysis of the root structures as the parameters cross phase boundaries.
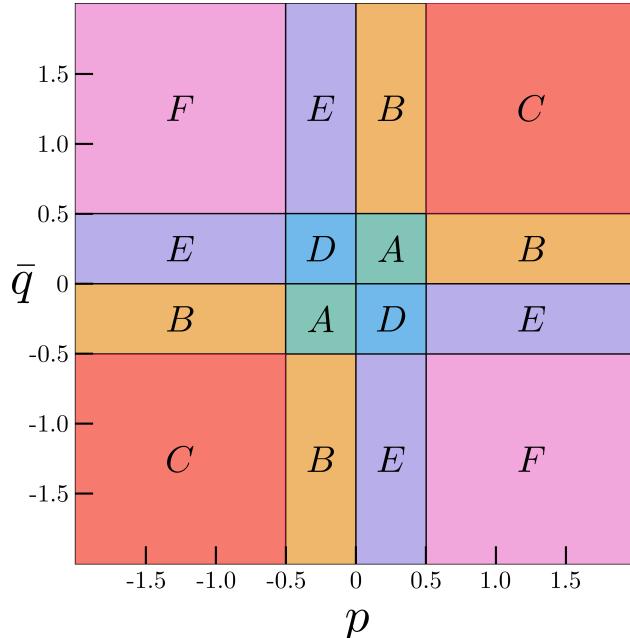
Figure 10: Phase diagram of zero-root configurations for the ground state in the $(p, \bar{q})$ plane of boundary parameters at $\eta = 1$.

From Fig. 10 and Table 2 we conclude that, for the ground state, the zero roots fall into three classes:

1. **Bulk strings:**
$$\pm(z_j + \eta) - \frac{\eta}{2}.$$

   All z_j are purely imaginary; these roots are the most numerous and form two straight lines parallel to the imaginary axis.

Table 2: The patterns of zero roots for the ground state in different regions. Roots related to z_j form the bulk strings; those tied to $|p|$ or $|\bar{q}|$ constitute boundary strings; z_0 and z_x are the additional roots.

Region	$\{z_i\}$
A	$\pm(z_j + \eta) - \frac{\eta}{2} \mid j = 1, \ldots, N-2,$ $\pm z_0 - \frac{\eta}{2},\ \pm(|p| + \frac{\eta}{2}) - \frac{\eta}{2},\ \pm(|\bar{q}| + \frac{\eta}{2}) - \frac{\eta}{2}$
B	$\pm(z_j + \eta) - \frac{\eta}{2} \mid j = 1, \ldots, N-2,$ $\pm z_0 - \frac{\eta}{2},\ \pm(\min(|p|, |\bar{q}|) + \frac{\eta}{2}) - \frac{\eta}{2},\ \pm(z_x + \frac{\eta}{2}) - \frac{\eta}{2}$
C	$\pm z_0 - \frac{\eta}{2},\ \pm(z_j + \eta) - \frac{\eta}{2} \mid j = 1, \ldots, N$
D	$\pm(z_j + \eta) - \frac{\eta}{2} \mid j = 1, \ldots, N-2,$ $\pm(z_x + \frac{\eta}{2}) - \frac{\eta}{2},\ \pm(|p| + \frac{\eta}{2}) - \frac{\eta}{2},\ \pm(|\bar{q}| + \frac{\eta}{2}) - \frac{\eta}{2}$
E	$\pm(z_j + \eta) - \frac{\eta}{2} \mid j = 1, \ldots, N,$ $\pm(\min(|p|, |\bar{q}|) + \frac{\eta}{2}) - \frac{\eta}{2}$
F	$\pm(z_x + \frac{\eta}{2}) - \frac{\eta}{2},\ \pm(z_j + \eta) - \frac{\eta}{2} \mid j = 1, \ldots, N$

2. **Boundary strings:**

- *p-boundary string:* $\pm\left(|p| + \dfrac{\eta}{2}\right) - \dfrac{\eta}{2}.$

- *$\bar{q}$-boundary string:* $\pm\left(|\bar{q}| + \dfrac{\eta}{2}\right) - \dfrac{\eta}{2}.$

Their positions are completely fixed by the boundary parameters.

3. **Additional roots:**

$$z_0 \text{ and } z_x.$$

z_0 is a purely imaginary number larger than the maximum of $\{z_j\}$, while z_x is a real number greater than $\frac{\eta}{2}$.

In fact, the zero-root structures shown in Fig. 10 and Table 2 are strictly valid only in the thermodynamic limit $N \to \infty$. For finite system sizes N, the zero-root structures exhibit small deviations. Numerical results indicate that the phase boundaries are typically slightly smaller than $\frac{\eta}{2}$, approaching $\frac{\eta}{2}$ as $N \to \infty$. Nevertheless, these deviations do not alter the overall structural characteristics of the zero roots, and the essential features can still be clearly observed even at finite lattice sizes.

In the following, we systematically analyze how zero-root structures evolve as boundary parameters are varied across the phase boundaries in the off-diagonal case. As the exact

transition boundary is uncertain at finite N, we provide several representative figures to illustrate the entire crossing process: The first and last figures correspond to the structures in two adjacent phase regions in Fig. 10, while the others depict structures close to the boundary.

We first discuss the transitions from Region A to Region D and from Region B to Region E. Exactly at $p = \bar{q} = 0$ the Hamiltonian energy diverges, and the root configuration changes discontinuously: $A \to D$ is realized by the mutual conversion of the additional roots $z_0 \to z_x$, whereas $B \to E$ corresponds to the pairwise annihilation of the additional roots. Away from this singular point the zero-root pattern still adheres to the regularity listed in Table 2 without any special deviation; hence no further elaboration is required.

Figure 11 illustrates how the root pattern evolves from Region A to Region B. In Region A the two characteristic structures identified in the phase diagram—the $\bar{q}$-boundary string and the p-boundary string—are clearly resolved Fig. 11(a). As $|p|$ increases toward the phase boundary, the two p-boundary strings separate horizontally and each coalesces with an additional root z_x (Fig. 11(b,c)). Once $|p|$ crosses the boundary, the original p-string roots are entirely replaced by the new pair z_x (Fig. 11(d)).

Fig. 12 illustrates the evolution of the zero roots during the transition from Region B to Region C. In Region B, the $\bar{q}$-boundary string can be clearly identified. As $|\bar{q}|$ increases, the $\bar{q}$-boundary string and additional root z_x gradually converge; upon entering Region C, the two roots merge into bulk strings.

Fig. 13 displays the evolution of zero roots as parameters change from Region D to Region E. This behavior closely resembles the transition observed between Regions B and C. In Region D, three characteristic roots are highlighted: p-boundary string, $\bar{q}$-boundary string, and the additional root z_x. As the parameter $|p|$ increases, p-boundary string and z_x gradually move closer together. At the limiting position, these two roots merge into bulk strings, while the $\bar{q}$-boundary string is preserved.

As shown in Fig. 14, the evolution from Region E to Region F is more similar to the case between Regions A and B. In Region E, the $\bar{q}$-boundary string is clearly visible (Fig. 14(a)). With increasing $|\bar{q}|$, this root shifts rightward and gradually transforms into an additional root z_x (Fig. 14(b, c)). Once $\bar{q}$ passes the phase boundary, the $\bar{q}$-boundary string is completely replaced by z_x (Fig. 14(d)).

(a) Region A

(b) Region A (near the boundary)

(c) Region B (near the boundary)
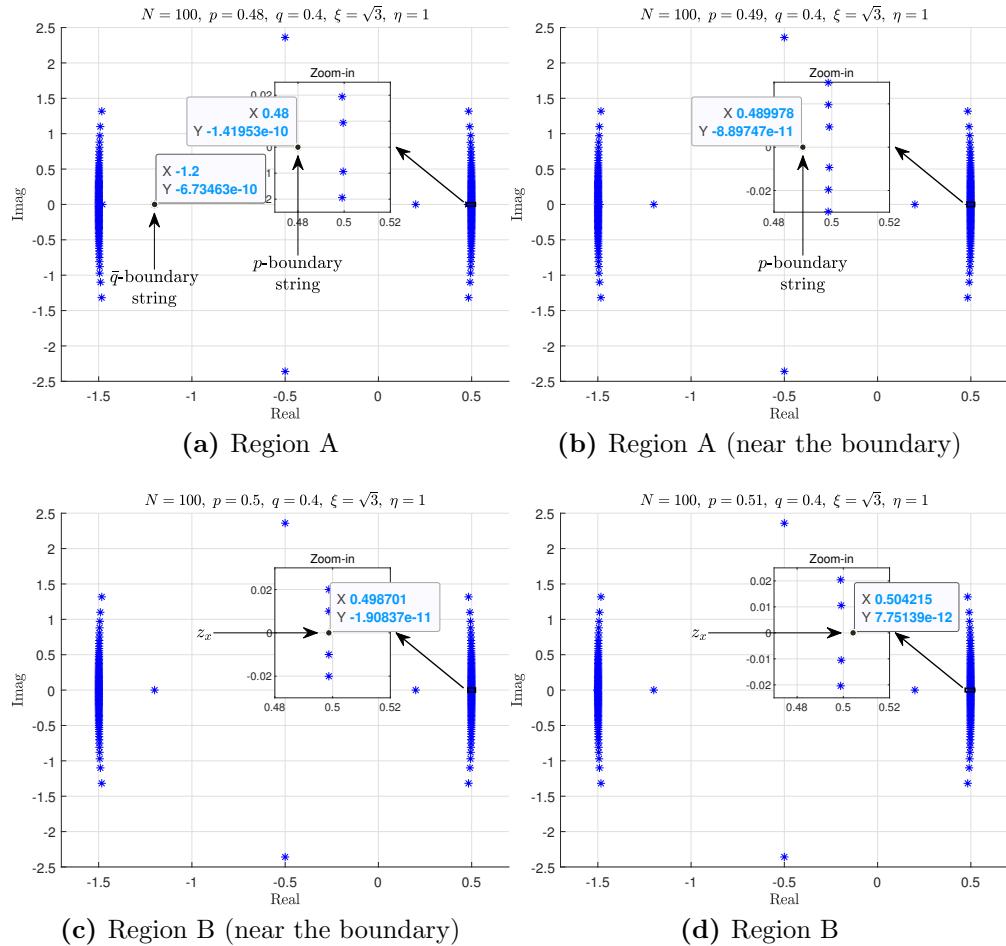
(d) Region B

Figure 11: Zero-root configurations as the boundary parameter crosses the A–B phase boundary. The parameters are fixed at $N = 100$, $q = 0.4$, $\xi = \sqrt{3}$, and $\eta = 1$, while p varies across the four panels: (a) $p = 0.48$ (Region A), (b) $p = 0.49$ (Region A, near the boundary), (c) $p = 0.5$ (Region B, near the boundary), (d) $p = 0.51$ (Region B).
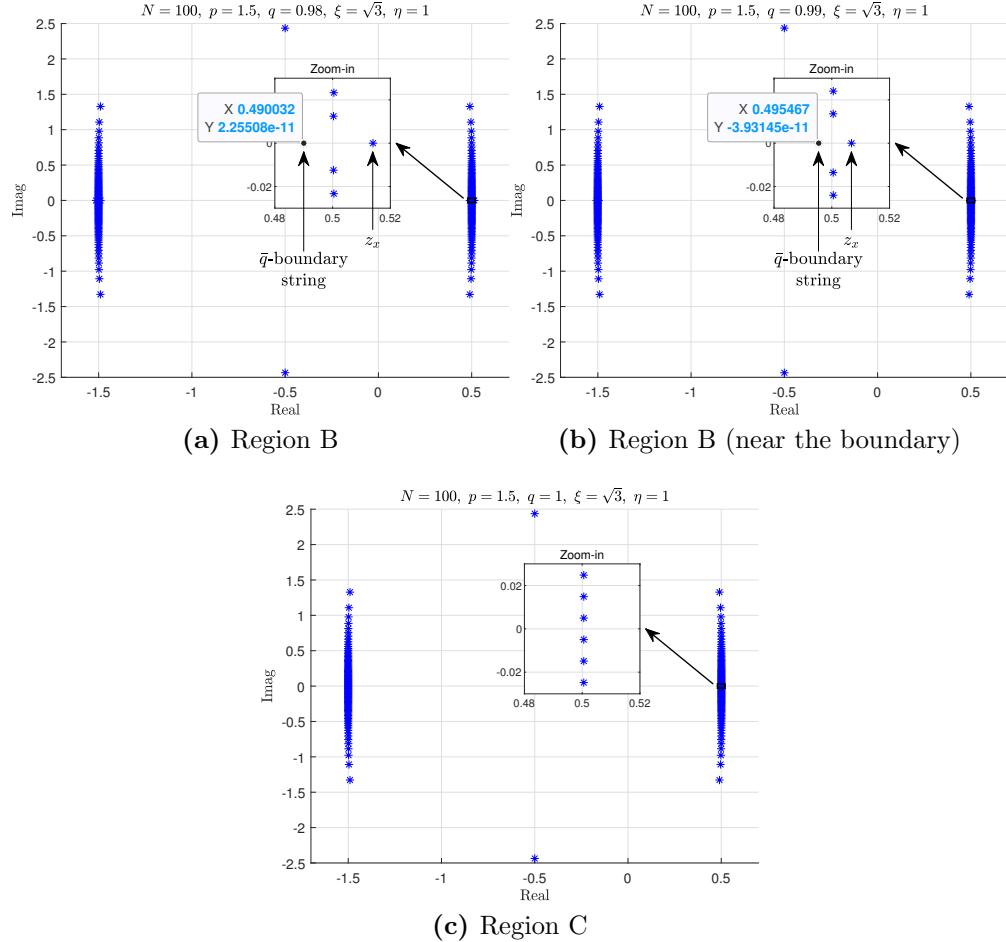
Figure 12: Zero-root configurations as the boundary parameter crosses the B–C phase boundary. The parameters are fixed as $N = 100$, $p = 1.5$, $\xi = \sqrt{3}$, and $\eta = 1$, while q varies across the three panels: (a) $q = 0.98$ (Region B), (b) $q = 0.99$ (Region B, near the boundary), (c) $q = 1$ (Region C).

(a) Region D

(b) Region D (near the boundary)
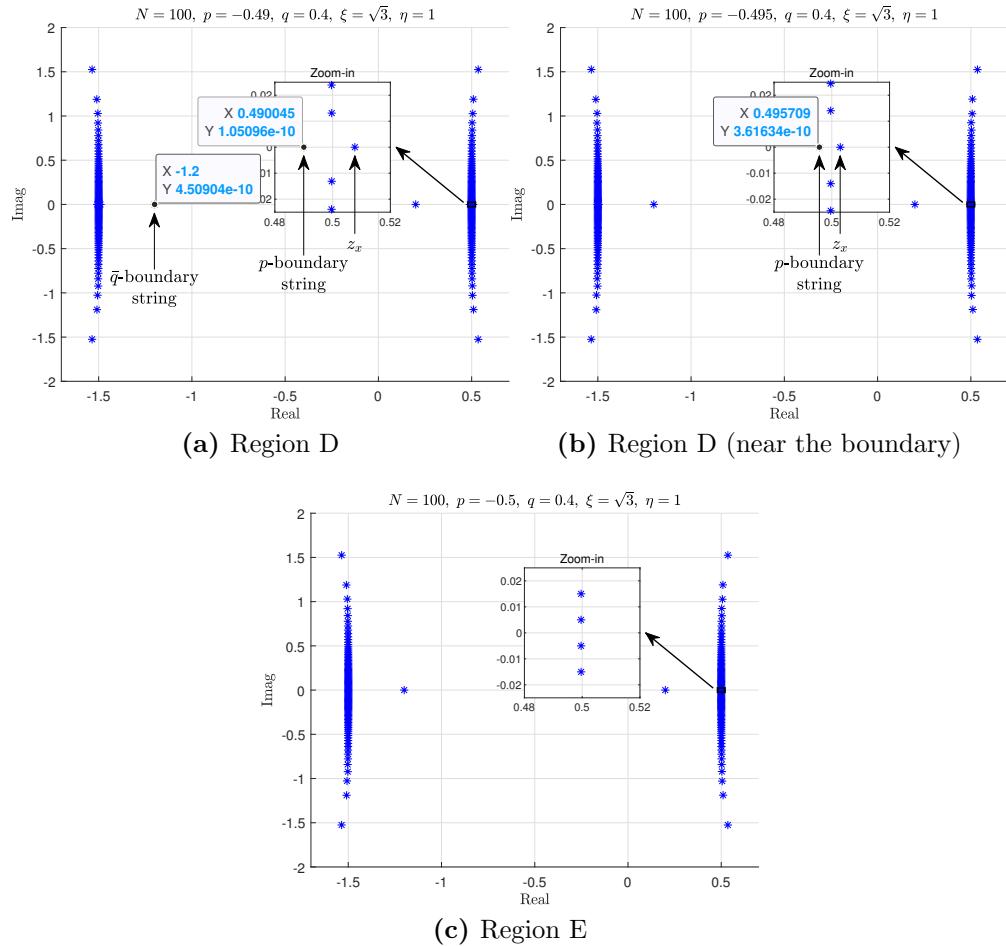
(c) Region E

Figure 13: Zero-root configurations as the boundary parameter crosses the D–E phase boundary. The parameters are fixed as $N = 100$, $q = 0.4$, $\xi = \sqrt{3}$, and $\eta = 1$, while p varies across the three panels: (a) $p = -0.49$ (Region D), (b) $p = -0.495$ (Region D, near the boundary), (c) $p = -0.5$ (Region E).

(a) Region E

(b) Region E (near the boundary)

(c) Region F (near the boundary)
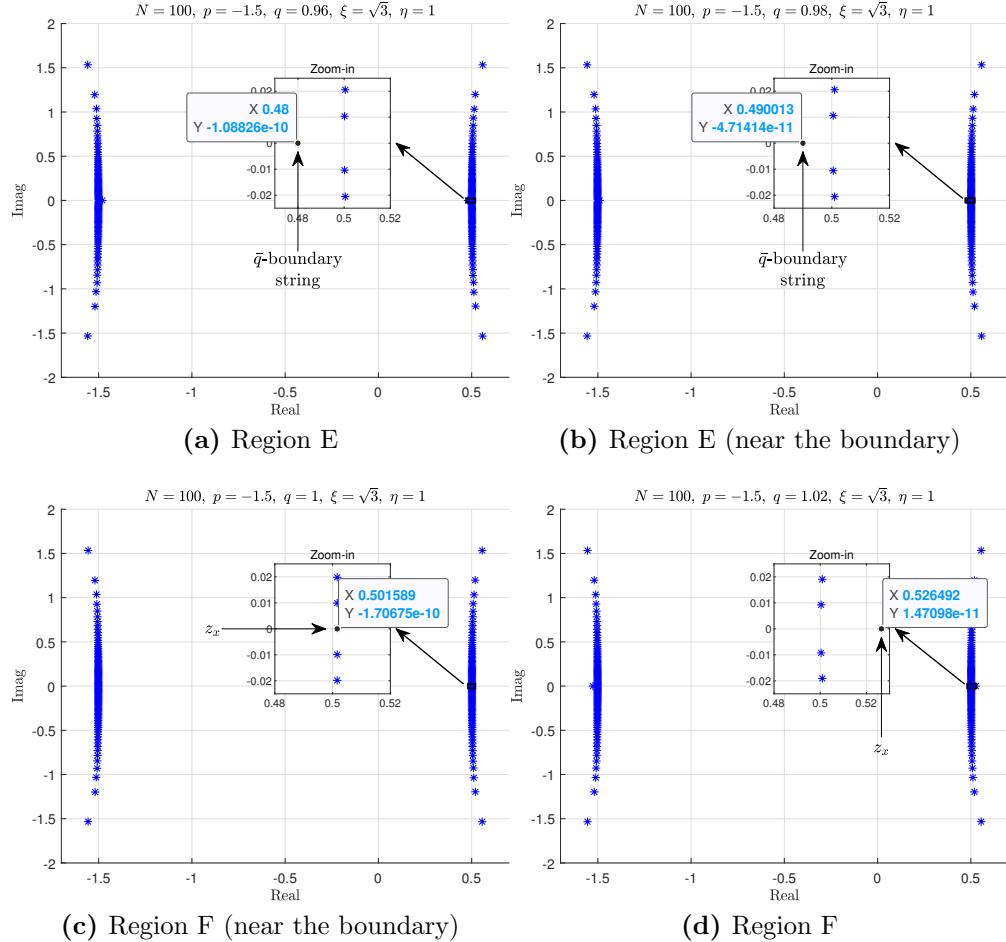
(d) Region F

Figure 14: Zero-root configurations as the boundary parameter crosses the E–F phase boundary. The parameters are fixed as $N = 100$, $p = -1.5$, $\xi = \sqrt{3}$, and $\eta = 1$, while q varies across the four panels: (a) $q = 0.96$ (Region E), (b) $q = 0.98$ (Region E, near the boundary), (c) $q = 1$ (Region F, near the boundary), (d) $q = 1.02$ (Region F).

5 Bethe roots

After obtaining $\Lambda(u)$, the Bethe roots can be determined by solving equations given in Eq. (2.22). The overall procedure follows a strategy similar to that described in Ref. [41]. However, since the $\Lambda(u)$ constructed from zero roots deviates slightly from the DMRG result, we use the DMRG-computed $\Lambda(u)$ to extract the Bethe roots.

We summarize the BA-DMRG procedure for obtaining the Bethe roots of $\Lambda(u)$ as follows:

1. Obtain the ground state MPS of the Hamiltonian.

2. Represent the transfer matrix $t(u)$ as an MPO.

3. Select a set of interpolation points $\{u_j\}$ and compute the corresponding eigenvalues $\bar{\Lambda}(u_j)$ of the transfer matrix in the ground state.

4. Express $\bar{Q}(u_j \pm \eta)$ as linear combinations of $\bar{Q}(u_j)$ using the Lagrange interpolation formula.

5. Construct and solve the linear system for $\bar{Q}(u_j)$ using the $T - Q$ relation (2.22).

6. Reconstruct the polynomial $\bar{Q}(u)$ using the obtained values of $\bar{Q}(u_j)$.

7. Determine the Bethe roots of $\bar{Q}(u)$ through numerical root-finding algorithms.

8. Verify the correctness of the obtained roots (the specific procedures and principles will be presented in the following sections); if verification fails, return to step 3 and use the current results as new interpolation points.

In steps 3-7, we perform the normalization by dividing both sides of the $T - Q$ relation (2.24) by u^{2N}. The related functions are then replaced by $\bar{\Lambda}(u) = \frac{\Lambda(u)}{u^{2N}}$ and $\bar{Q}(u) = \frac{Q(u)}{u^{2N}}$. This normalization is necessary because, during the computation, some values of $\Lambda(u)$ may exceed the numerical range of the machine. Therefore, we normalize each variable throughout the process to ensure numerical stability.

In step 4, $Q(u)$ is a degree-$2N$ polynomial with a unit leading coefficient (2.23), and hence it can be uniquely specified by its values at $2N$ distinct points. We select $2N$ values $Q(u_j)$ as unknowns and use Lagrange interpolation to express $Q(u_j \pm \eta)$ as linear combinations of

$Q(u_j)$. Specifically, the interpolation takes the form

$$Q(u) = \prod_{j=1}^{2N}(u - u_j) + \sum_{j=1}^{2N} Q(u_j) \prod_{\substack{1 \leq k \leq 2N \\ k \neq j}} \frac{u - u_k}{u_j - u_k}. \tag{5.1}$$

In step 8, if verification fails, iteration is needed: return to step 3 and use the current results as new interpolation points, repeating this process until the desired accuracy is achieved.

It is worth emphasizing that, unlike Ref. [41], where $\Lambda(u)$ is computed using high-precision arithmetic (e.g., VPA) and thus achieves significantly more digits than the sixteen available in standard double precision, the $\Lambda(u)$ obtained from the DMRG does not reach such accuracy. High-precision DMRG implementations in ITensor are still immature; consequently, all DMRG calculations in this study are performed in double precision and are further limited by the prescribed convergence tolerance. In the homogeneous case, numerical verification shows that, under the parameter settings adopted in this work, the relative error of $\Lambda(u)$ at $N = 100$ computed by DMRG is no worse than 10^{-10}. Consequently, the $2N$ interpolation nodes must be judiciously placed to guarantee numerical stability; otherwise, the iterative solver struggles to converge. We should select the interpolation points for large lattices by following the known distribution pattern of Bethe roots on small lattices.

5.1 Ground state solution with U(1) symmetry

For the homogeneous case with $\xi = 0$, it has already been mentioned in Sec. 4.1 that by using Eq. (4.5), the Bethe roots can be accurately determined even for large N. The Bethe roots obtained from the BA-DMRG method can then be compared with these results to verify the validity of our approach.

As mentioned in Sec. 4.1, in the homogeneous case, the $Q(u)$ function for the ground state reduces from a $2N$-th degree polynomial to an N-th degree polynomial. Starting from the initial N interpolation nodes $\{u_j\}_{j=1}^{N}$, defined as $\{x_j, -x_j - \eta \mid j = 1, 2, \ldots, \frac{N}{2}\}$ with $x_j = -\frac{\eta}{2} + \frac{i}{N}j^k$ and $k \in [1, 1.1]$, and performing iterative refinements, we obtain the comparison illustrated in Fig. 15. The maximum absolute error between the corresponding roots is 4.9×10^{-11}.

These results show that, even for large systems at $\xi = 0$, the Bethe roots obtained from the logarithmic BAEs coincide almost perfectly with those delivered by BA-DMRG. Such

(a) Global configuration of Bethe roots   **(b)** Enlarged view of the central region
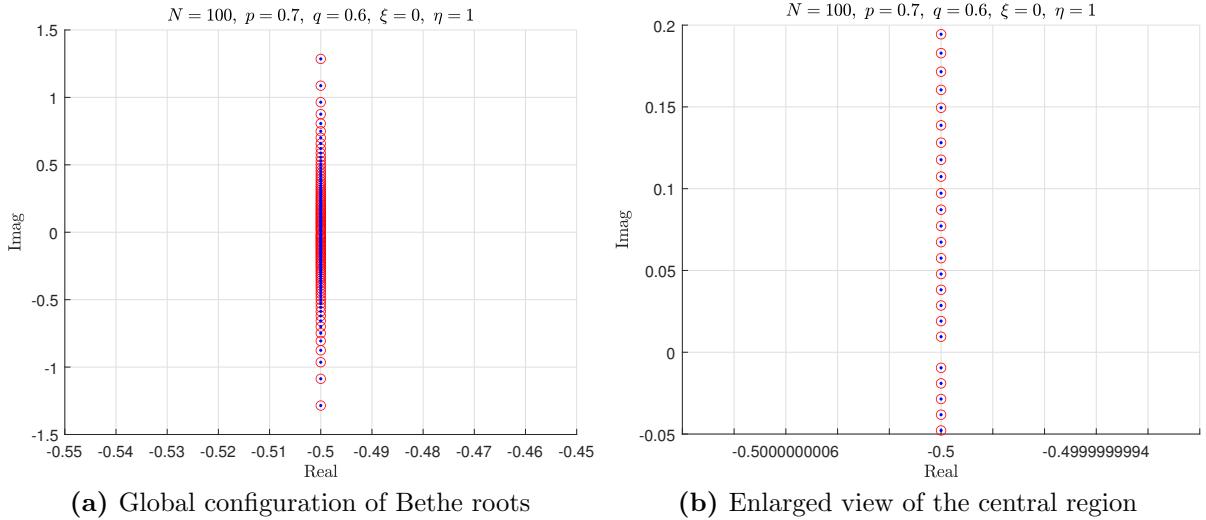
Figure 15: Distribution of Bethe roots in the complex plane with parameters $N = 100$, $p = 0.7$, $q = 0.6$, $\xi = 0$, and $\eta = 1$. Red circles denote Bethe roots obtained by solving the logarithmic form of the BAEs, while blue dots represent those computed using the BA-DMRG method.

consistency confirms the feasibility of the BA-DMRG approach as a reliable numerical tool for extracting Bethe roots. Together, these findings provide strong evidence that our approach is both robust and well suited for extension to more general inhomogeneous systems.

5.2   Ground state solution without U(1) symmetry

In the inhomogeneous case, the ground-state $Q(u)$ becomes a degree-$2N$ polynomial, twice the degree of the homogeneous case. The corresponding Bethe-root pattern exhibits a more intricate structure. Together these two effects push the solution difficulty sharply upward, so the attainable lattice size N is therefore limited compared with the homogeneous case [4].

Following the same strategy as in the homogeneous case, but noting that $Q(u)$ is now a $2N$-th degree polynomial, the interpolation scheme needs to be modified accordingly. Specifically, the $2N$ interpolation nodes $\{u_j\}_{j=1}^{2N}$ are constructed as $\{x_j, -x_j - \eta \mid j = 1, 2, \ldots, N\}$. The first $\frac{N}{2}$ $\{x_j\}$ nodes are defined as $x_j = -\frac{\eta}{2} + \frac{i}{N}j^k$, where $k \in [1, 1.1]$, while the remaining $\frac{N}{2}$ $\{x_j\}$ nodes are specified as $x_j = j + t$, with $j = \frac{N}{2} + 1, \frac{N}{2} + 2, \ldots, N$ and $t \in (0, \frac{N}{4})$. In addition, another effective choice for the remaining $\frac{N}{2}$ nodes is $x_j = t + (j - \frac{N}{2})i - \frac{N}{4}i$, where t is chosen around $\frac{N}{4}$. With the interpolation nodes placed as above, convergence is achieved

---

[4]If the precision of BA-DMRG data could be raised beyond 16 significant digits, high-accuracy Bethe roots for larger systems would become accessible.

in fewer than 10 iterations.

(a) Global configuration of Bethe roots   **(b)** Enlarged view of the central region
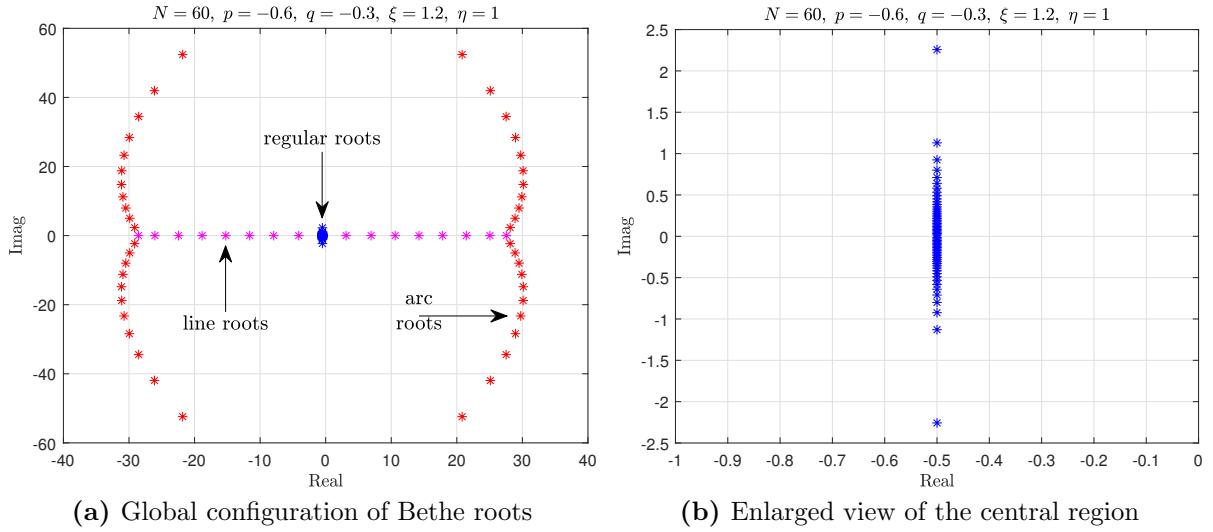
Figure 16: Distribution of Bethe roots in the complex plane with parameters $N = 60$, $p = -0.6$, $q = -0.3$, $\xi = 1.2$, and $\eta = 1$. The blue, purple, and red markers denote the regular, line, and arc roots, respectively.

With the interpolation nodes detailed above, we compute the Bethe roots for the non-U(1)-symmetric case; the resulting configuration is shown in Fig. 16. We find that the ground-state Bethe roots fall into three classes:

1. **Regular roots:**

   - *Central roots:* $z_j - \eta/2$, with all z_j purely imaginary;

   - *Boundary strings:* $\pm(p - \eta/2) - \eta/2$ and $\pm(\bar{q} - \eta/2) - \eta/2$, whose positions are fixed solely by the boundary parameters.

   There are precisely N or $N - 2$ regular roots; their distribution mirrors that of the homogeneous chain.

2. **Line roots:** A set of purely real roots.

3. **Arc roots:** At the outer ends of the line roots, complex roots bifurcate into symmetric arcs in the upper and lower half-planes.

For the present parameter set the pattern coincides with the periodic-boundary results of Ref. [41] obtained from the inhomogeneous $T - Q$ relation. Other parameter regions reveal richer structures, most notably the **Paired-line roots** introduced in the next subsection.

Now, an important task is to verify the correctness of the obtained Bethe roots. Among the available data, the only quantity that can be regarded as fully reliable is $\Lambda(u)$ calculated by the DMRG method. Therefore, we substitute the Bethe roots into the $T - Q$ relation to compute a new quantity $\Lambda'(u)$ and then compare it with the DMRG result $\Lambda(u)$. The comparison is carried out precisely at the positions of the Bethe roots.

From Eq. (2.24), the $T - Q$ relation can be expressed as

$$\Lambda(u) = \frac{F(u)}{Q(u)}, \tag{5.2}$$

where

$$\begin{aligned}
F(u) = & \frac{2(u + \eta)^{2N+1}}{2u + \eta}(u + p)[(1 + \xi^2)^{\frac{1}{2}}u + q]Q(u - \eta) \\
& + \frac{2u^{2N+1}}{2u + \eta}(u - p + \eta)[(1 + \xi^2)^{\frac{1}{2}}(u + \eta) - q]Q(u + \eta) \\
& + 2[1 - (1 + \xi^2)^{\frac{1}{2}}][u(u + \eta)]^{2N+1}.
\end{aligned} \tag{5.3}$$

For the Bethe roots $\{\lambda_j \mid j = 1, \ldots, N\}$, both $F(\lambda_j) = 0$ and $Q(\lambda_j) = 0$ hold. Thus, one obtains

$$\Lambda(\lambda_j) = \lim_{u \to \lambda_j} \frac{F(u)}{Q(u)} = \frac{F'(\lambda_j)}{Q'(\lambda_j)}, \tag{5.4}$$

where $F'(u)$ and $Q'(u)$ denote derivatives with respect to u, and both derivatives can be evaluated straightforwardly.

By comparing the values of $\Lambda(\lambda_j)$ obtained from the Bethe roots with those of $\Lambda(\lambda_j)$ computed via the DMRG method, the relative error is defined as

$$\varepsilon_j = \frac{|\Lambda_{DMRG}(\lambda_j) - \Lambda_{Bethe}(\lambda_j)|}{|\Lambda_{DMRG}(\lambda_j)|}. \tag{5.5}$$

The numerical results show that the maximum relative error is about 0.007759%, which demonstrates that the obtained Bethe roots are sufficiently accurate. This also indicates that the procedure is numerically stable. Further detailed data are provided in Appendix D.

In addition, according to the BAEs (2.25), we further verify the correctness of the obtained Bethe roots. The BAEs can be rewritten in the form

$$A(\lambda_j) = -B(\lambda_j) - C(\lambda_j), \qquad j = 1, \ldots, N, \tag{5.6}$$

where

$$A(\lambda) = \left(\frac{\lambda + \eta}{\lambda}\right)^{2N+1} \frac{(\lambda + p)\left[(1 + \xi^2)^{\frac{1}{2}}\lambda + q\right]}{(\lambda - p + \eta)\left[(1 + \xi^2)^{\frac{1}{2}}(\lambda + \eta) - q\right]}, \tag{5.7}$$

$$B(\lambda) = \frac{Q(\lambda + \eta)}{Q(\lambda - \eta)}, \tag{5.8}$$

$$C(\lambda) = \frac{\left[1 - (1 + \xi^2)^{\frac{1}{2}}\right](2\lambda + \eta)(\lambda + \eta)^{2N+1}}{(\lambda - p + \eta)\left[(1 + \xi^2)^{\frac{1}{2}}(\lambda + \eta) - q\right]Q(\lambda - \eta)}. \tag{5.9}$$

Define

$$G(u) = \frac{A(u) + C(u)}{-B(u)}. \tag{5.10}$$

For $G(u) = 1$, the BAEs are satisfied exactly. We have computed all values of $G(\lambda_j)$; the largest deviation from unity is $0.9999748 - 0.0000059i$, and the detailed numerical results are provided in Appendix D. These validation data further confirm the accuracy of the Bethe roots.

5.3 Structure of the Bethe roots

Unlike the zero-root case, the number of Bethe roots in the ground state already differs between the $U(1)$-symmetric and $U(1)$-symmetry-broken cases, leading to markedly distinct root distributions in the two situations. Since the Bethe roots in the homogeneous case exhibit simple behavior, this section focuses on analyzing the structure of the inhomogeneous Bethe roots. From the BAEs (2.25), it is evident that p and $\bar{q}$ enter the equations symmetrically. Therefore, it suffices to analyze the variation with respect to only one of these parameters. Given the considerable complexity of their configurations, we restrict our discussion here to the characteristic changes of the Bethe roots as p vary and $\bar{q}$ fixed.

As p varies, we systematically investigate the resurgence of $U(1)$ symmetry while $|p|$ is continuously increased from finite values to infinity. In the asymptotic limit $|p| \to \infty$, the system recovers $U(1)$ symmetry: exactly N Bethe roots diverge to infinity, while the remaining N roots condense onto the vertical contour $\text{Re}(u) = -0.5$ (Fig. 15). We now systematically track the reorganization of the Bethe-root configuration from the generic inhomogeneous distribution shown in Fig. 16 to the regularized pattern exhibited in Fig. 15 under the continuous amplification of $|p|$. The evolution exhibits two distinct paradigms, contingent upon the sign of the boundary parameter p.

5.3.1 $p > 0$ case

In this subsection we focus on the case where the boundary parameter satisfies $p > 0$. For clarity, we first illustrate the case with $\bar{q} = 0.35$; the negative-$\bar{q}$ scenario is qualitatively

similar and its minor differences will be summarized at the end of this subsection. To establish a baseline for the subsequent analysis, we first present the initial structure of the Bethe roots for small p. For $0 < p < \frac{\eta}{2}$ or $0 < \bar{q} < \frac{\eta}{2}$, the Bethe roots exhibit a clear **boundary-string** configuration that is identical to the one appearing in the homogeneous case. The endpoints of these boundary strings are located at $\pm(p - \frac{\eta}{2}) - \frac{\eta}{2}$ or $\pm(\bar{q} - \frac{\eta}{2}) - \frac{\eta}{2}$, respectively, as illustrated in Fig. 17. We classify boundary strings as regular roots defined in this work.

(a) Global configuration of Bethe roots   **(b)** Enlarged view of the central region
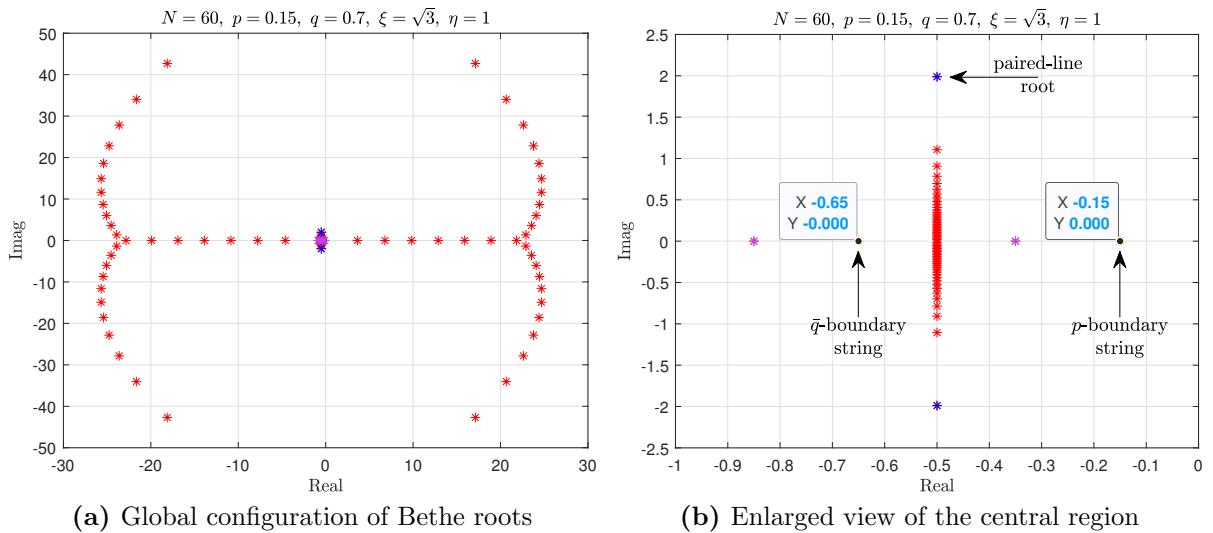
Figure 17: Distribution of Bethe roots in the complex plane with parameters $N = 60$, $p = 0.15$, $q = 0.7$, $\xi = \sqrt{3}$, and $\eta = 1$. The purple points represent the boundary strings, and the blue points correspond to the paired-line roots, which here appear as a single conjugate pair.

As p increases, both the line roots and the arc roots gradually move toward the central roots. During this process, certain arc roots approach the real axis and transform into line roots. Meanwhile, conjugate pairs aligned along directions parallel to the central roots begin to appear. They initially occupy the positions of the line roots closest to the central roots, and this replacement then progresses outward to the more distant line roots. We refer to these conjugate pairs as the **paired-line roots**, and such roots occur only when either $p > 0$ or $\bar{q} > 0$.

Quantisation rule. The number of paired-line pairs increases in unit steps. When $|\bar{q}|$ is small, and as p increases, each time the combination $p + \bar{q}$ reaches an integer multiple of η,

that is, $p + \bar{q} = k\eta$ with $k \in \mathbb{Z}^+$, one additional pair of paired-line roots appears. For $\bar{q} > 0$, the total number of paired-line root pairs is therefore given by $\max\{1, \lfloor p + \bar{q} \rfloor\}$, where $\lfloor \rfloor$ denotes the floor function. The number of regular roots remains unchanged and is always equal to N.

This minimal configuration is shown in Fig. 17, where the single paired-line root pair lies on the vertical contour $\text{Re}(u) = -0.5$. As concrete illustrations of this pattern, we present the cases $p = 1.75$ and $p = 5.55$, where the numbers of paired-line root pairs are two and five, respectively, as shown in Figs. 18 and 19.

(a) Global configuration of Bethe roots   **(b)** Enlarged view of the central region
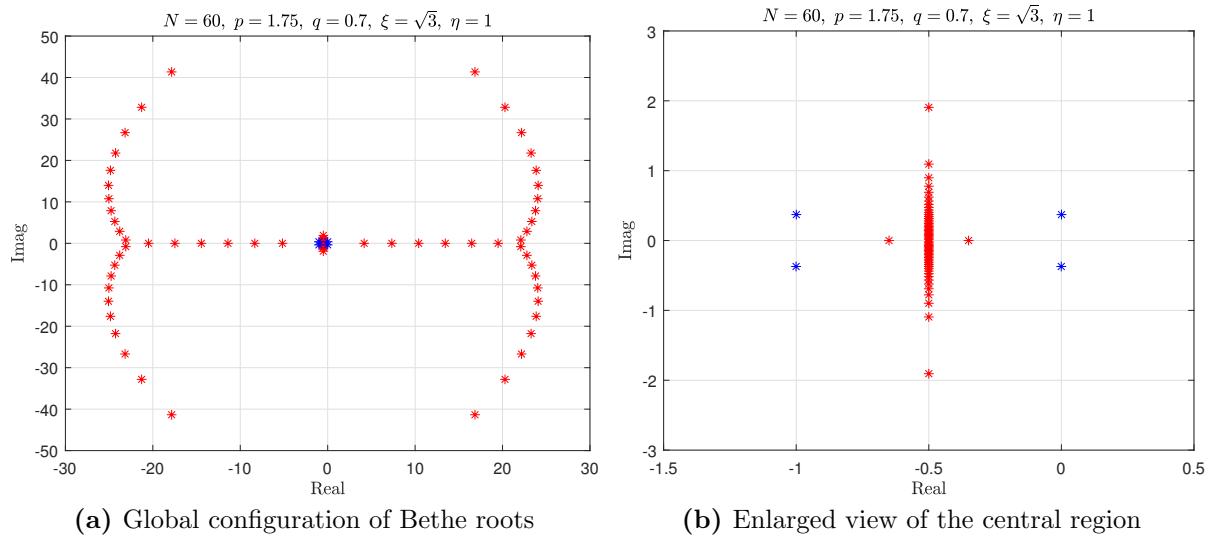
Figure 18: Distribution of Bethe roots in the complex plane with parameters $N = 60$, $p = 1.75$, $q = 0.7$, $\xi = \sqrt{3}$, and $\eta = 1$. The blue points correspond to the paired-line roots, which appear here as two paired-line root pairs.

The increase in the number of paired-line root pairs occurs within an extremely narrow interval, and within this crossover region the changes in the Bethe-root configuration are highly intricate. As the system size N grows, the width of this interval becomes even smaller, indicating that the crossover behavior is dominated by finite-size effects. We provide a detailed illustration of the crossover behavior in Appendix E.

After all line roots have converted into paired-line root pairs, further increasing p drives the two members of each paired-line root to split apart: one drifts upward and the other downward, moving away from the real axis, as illustrated in Fig. 20.

As p is further increased, the arc roots and the paired-line root pairs formed by the N Bethe roots move away from the center toward infinity, while the N regular roots remain

(a) Global configuration of Bethe roots

(b) Enlarged view of the central region
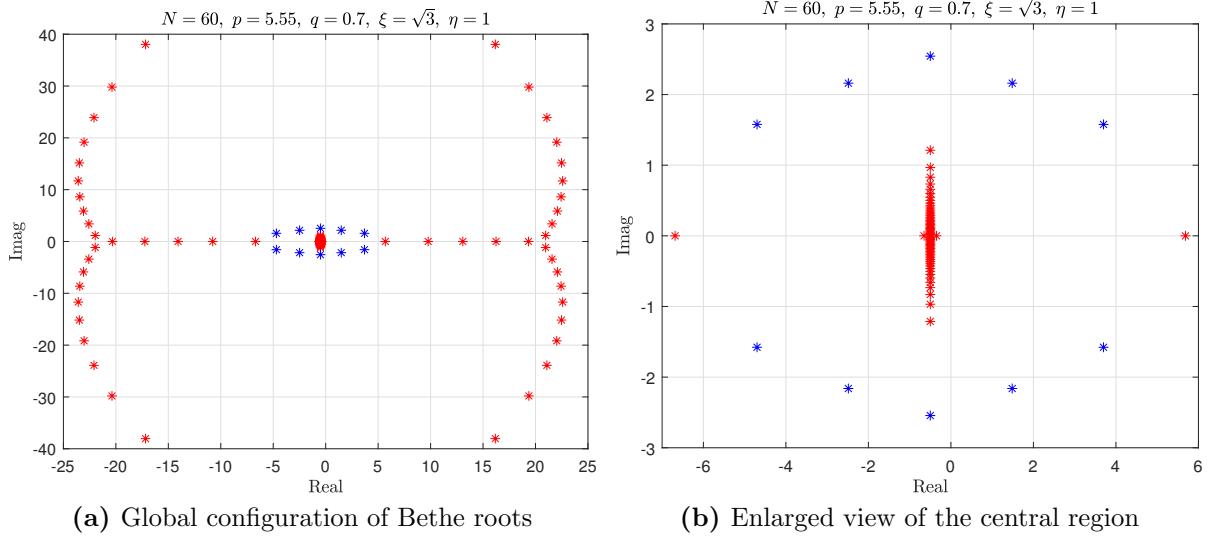
Figure 19: Distribution of Bethe roots in the complex plane with parameters $N = 60$, $p = 5.55$, $q = 0.7$, $\xi = \sqrt{3}$, and $\eta = 1$. The blue points correspond to the paired-line roots, which appear here as five paired-line root pairs.

(a) Global configuration of Bethe roots

(b) Enlarged view of the central region
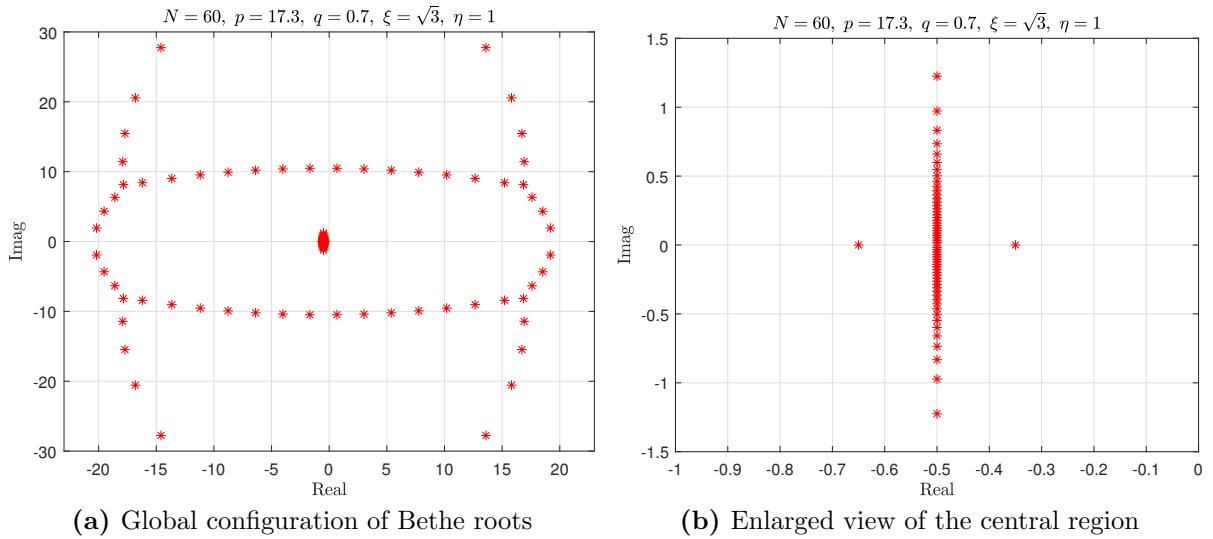
Figure 20: Distribution of Bethe roots in the complex plane with parameters $N = 60$, $p = 17.3$, $q = 0.7$, $\xi = \sqrt{3}$, and $\eta = 1$.

at the center. This behavior arises because, for the Hamiltonian (2.14), when either p or q tends to infinity, the magnetic field at one boundary approaches zero and the previously broken $U(1)$ symmetry is restored. At this point, the Bethe Ansatz equations are expected to reduce to those of the homogeneous case. By setting the boundary parameters to be identical-so that q' in the homogeneous case equals $\bar{q}$ in the inhomogeneous case-the central Bethe roots obtained in the inhomogeneous case can be directly compared with those of the homogeneous case (see Fig. 21). The two sets of roots show only negligible discrepancies, which further demonstrates the validity of the algorithm.

(a) Global configuration of Bethe roots   **(b)** Enlarged view of the central region
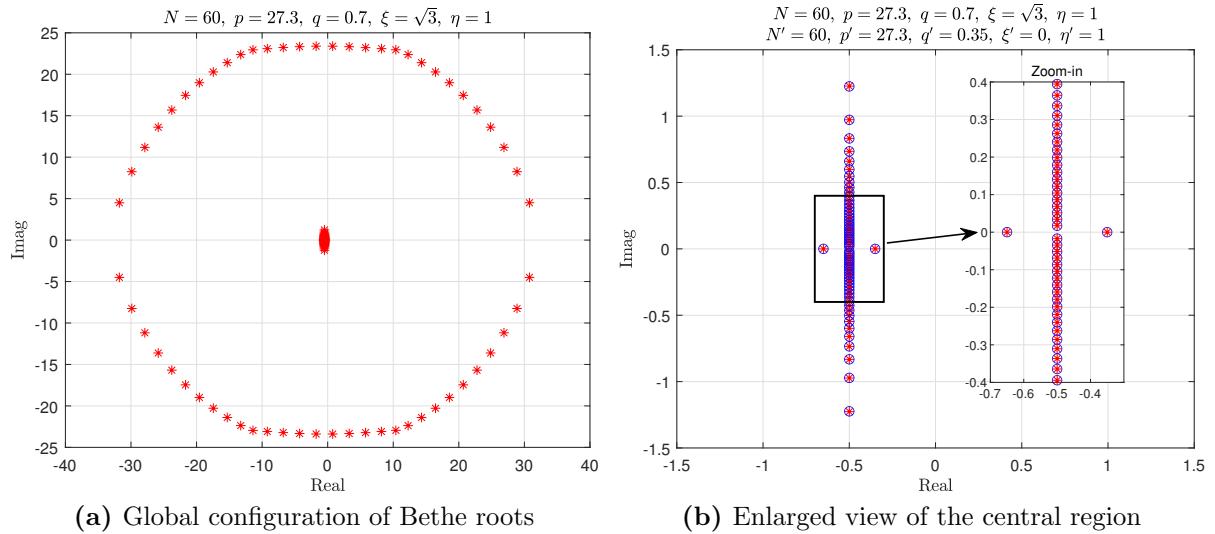
Figure 21: Distribution of Bethe roots in the complex plane with parameters $N = 60$, $p = 27.3$, $q = 0.7$, $\xi = \sqrt{3}$, and $\eta = 1$. Blue circles in panel (b) indicate the Bethe roots obtained in the homogeneous case with parameters $N' = 60$, $p' = 27.3$, $q' = 0.35$, $\xi' = 0$, and $\eta' = 1$.

For negative $\bar{q}$, the evolution of the Bethe-root structure with increasing p closely parallels the positive-$\bar{q}$ case, with only two quantitative differences: (i) the number of paired-line root pairs is $\max\{1, \lfloor p+\bar{q}+1 \rfloor\}$; (ii) the number of regular roots is $N-2$ at small p, but once all line roots have transformed into paired-line root pairs, the number of regular roots becomes N and remains fixed at this value throughout the subsequent evolution. Apart from these differences, the rest of the analysis remains unchanged.

5.3.2 $p < 0$ case

When $p < 0$ and increase $|p|$, the structural change is comparatively simpler, and the overall evolution is identical regardless of the sign of $\bar{q}$. For consistency with the previous subsection, we likewise set $\bar{q} = 0.35$ in the following analysis.

(a) Global configuration of Bethe roots   **(b)** Enlarged view of the central region
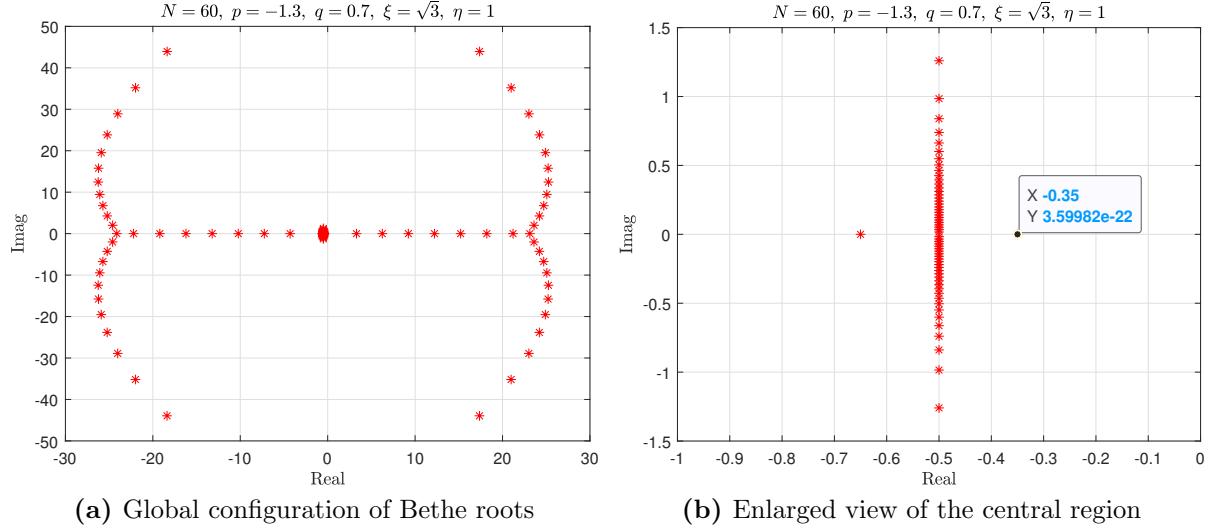
Figure 22: Distribution of Bethe roots in the complex plane with parameters $N = 60$, $p = -1.3$, $q = 0.7$, $\xi = \sqrt{3}$, and $\eta = 1$.

In contrast to the case of positive p, as the absolute value of the parameter increases, the inner line roots move outward away from the center, while the outermost line roots remain almost unchanged, as shown from Fig. 22 to Fig. 23.

When the two outermost line roots on the real axis approach their limiting separation, they separate from that position and become part of the arc roots, as shown in Fig. 24.

Eventually, all line roots transform into the arc roots and continue to move toward infinity, totaling N, while the N regular roots remain at the center. As in the previous case, the Hamiltonian regains $U(1)$ symmetry, and the Bethe Ansatz equations reduce to the homogeneous form. A comparison of these two situations, shown in Fig. 25, exhibits excellent agreement.

6 Conclusion

By combining tensor-network techniques with the Bethe Ansatz, we have performed a systematic study of the open XXX spin-$\frac{1}{2}$ chain in the large-lattice case. We accurately compute

(a) Global configuration of Bethe roots

(b) Enlarged view of the region where the structural change occurs
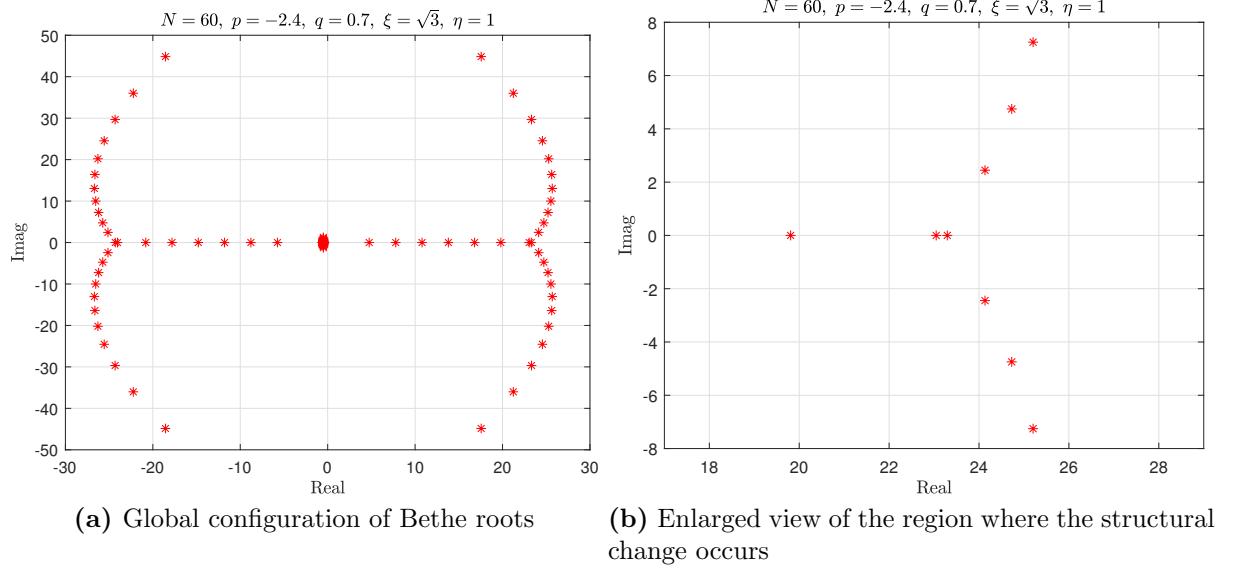
Figure 23: Distribution of Bethe roots in the complex plane with parameters $N = 60$, $p = -2.4$, $q = 0.7$, $\xi = \sqrt{3}$, and $\eta = 1$.

(a) Global configuration of Bethe roots

(b) Enlarged view of the region where the structural change occurs
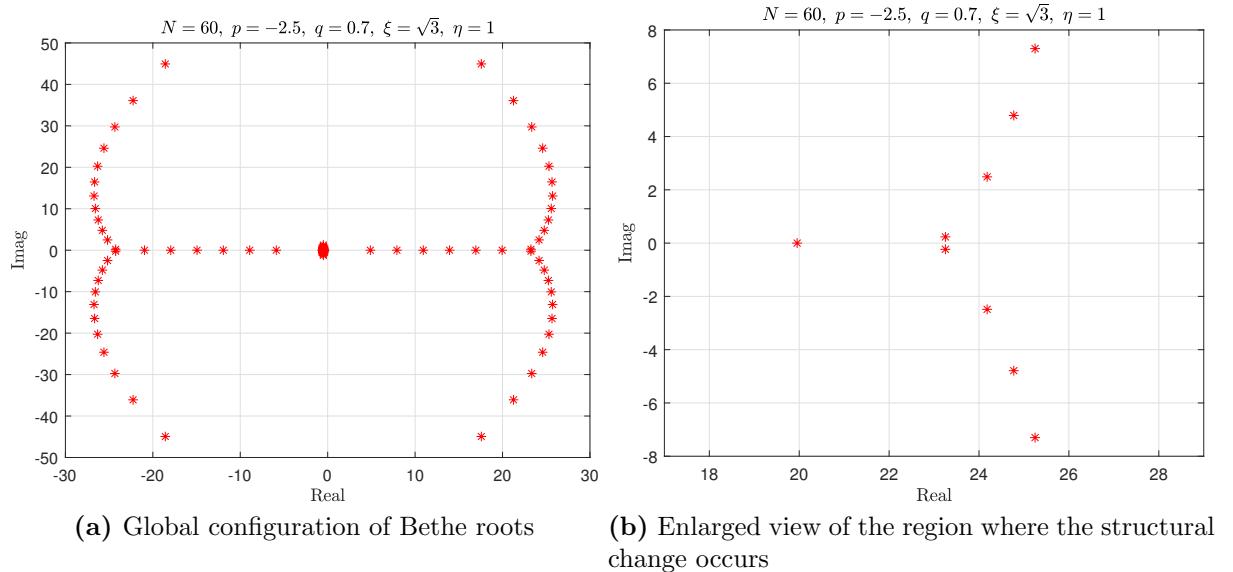
Figure 24: Distribution of Bethe roots in the complex plane with parameters $N = 60$, $p = -2.5$, $q = 0.7$, $\xi = \sqrt{3}$, and $\eta = 1$.

(a) Global configuration of Bethe roots

(b) Enlarged view of the central region
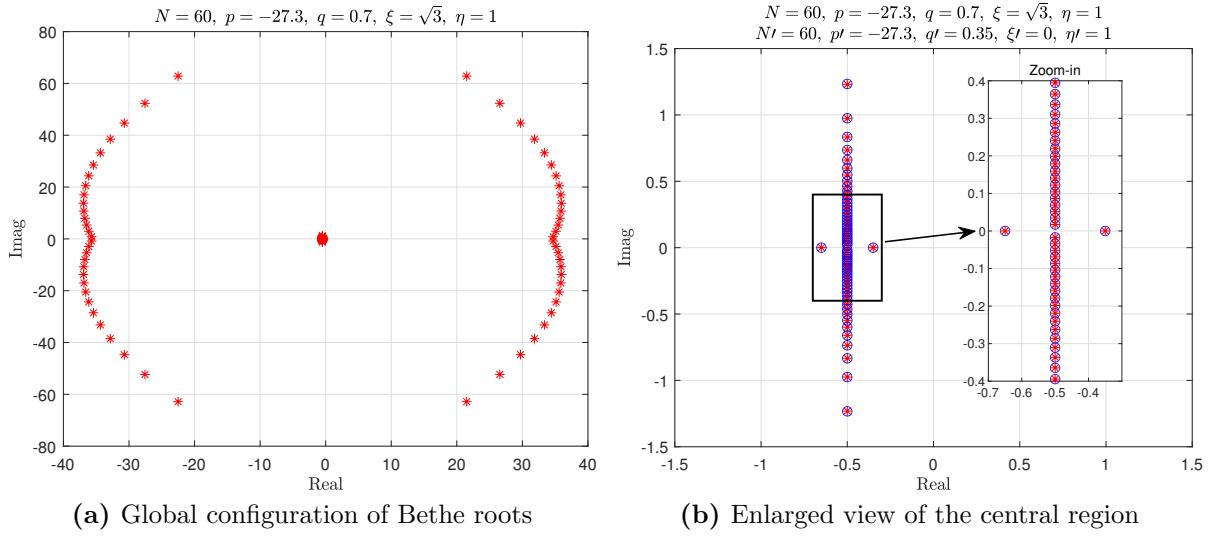
Figure 25: Distribution of Bethe roots in the complex plane with parameters $N = 60$, $p = -27.3$, $q = 0.7$, $\xi = \sqrt{3}$, and $\eta = 1$. Blue circles in panel (b) indicate the Bethe roots obtained in the homogeneous case with parameters $N' = 60$, $p' = -27.3$, $q' = 0.35$, $\xi' = 0$, and $\eta' = 1$.

both zero roots and Bethe roots for the ground-state eigenvalue of the transfer matrix; notably, the $U(1)$ symmetry-broken sector at large system sizes is now accessible and validated by rigorous complex-analysis checks.

We confirmed that, irrespective of whether $U(1)$ symmetry is preserved or broken, the zero-root pattern remains remarkably simple. At large N we verified the phase diagram proposed in Ref. [40] and tracked in detail how the zero roots evolve when parameters are driven across phase boundaries.

In the regime of broken $U(1)$ symmetry, the Bethe roots naturally resolve into four geometric classes—regular, line, paired-line, and arc. As the boundary parameters are sent from finite values to infinity, the system's $U(1)$ symmetry is gradually restored, and we systematically track the evolutionary trajectories and transition rules of these four Bethe-root classes across the entire crossover.

In the symmetry-broken regime the zero-root configuration is orders of magnitude simpler than the full Bethe-root set, offering an efficient shortcut for analytical calculations. The present accuracy is limited by the precision of the transfer-matrix eigenvalues provided by DMRG; any future improvement will immediately extend the approach to even larger systems. The numerical framework established here can be applied straightforwardly to excited

states and to other quantum integrable models on large lattices.

Acknowledgments

We would like to thank Prof. Y. Wang for his valuable discussions and continuous encouragement. Yi Qiao special thanks to Dr. K. Wang for helpful discussions and suggestions on tensor-network numerics. The financial supports from the National Key R&D Program of China (Grant No.2021YFA1402104), the National Natural Science Foundation of China (Grant Nos. 12547107, 12434006, 12305005, 12247103 and 12105221), Major Basic Research Program of Natural Science of Shaanxi Province (Grant Nos. 2021JCW-19 and 2017ZDJC-32), Young Talent Fund of Xi'an Association for Science and Technology (Grant No. 959202313086), and Shaanxi Fundamental Science Research Project for Mathematics and Physics (Grant No. 22JSZ005).

A MPO Representation of the Transfer Matrix

To facilitate the derivation of analytical expressions, the R-matrix in Eq. (2.1) can be rewritten as a 2×2 operator-valued matrix acting on the space labeled by 0:

$$R_{0,j}(u) := \begin{pmatrix} a_j(u) & b_j(u) \\ c_j(u) & d_j(u) \end{pmatrix}_0. \tag{A.1}$$

For the present R-matrix, $R_{j,0}(u) = R_{0,j}(u)$. Using the projection notation introduced later, the matrix elements in the basis $\{|0\rangle_0, |1\rangle_0\}$ read

$$a_j(u) = R_{0,j}(u)\big|_0^0 = \begin{pmatrix} u + \eta & 0 \\ 0 & u \end{pmatrix}_j,$$

$$b_j(u) = R_{0,j}(u)\big|_1^0 = \begin{pmatrix} 0 & 0 \\ \eta & 0 \end{pmatrix}_j,$$

$$c_j(u) = R_{0,j}(u)\big|_0^1 = \begin{pmatrix} 0 & \eta \\ 0 & 0 \end{pmatrix}_j, \tag{A.2}$$

$$d_j(u) = R_{0,j}(u)\big|_1^1 = \begin{pmatrix} u & 0 \\ 0 & u + \eta \end{pmatrix}_j.$$

The analytical derivation is presented below. For clarity we set $N = 3$, with the general case obtained analogously. For simplicity, we will omit the parameter (u) in the subsequent

derivation:

$$\text{tr}_0\left\{K_0^+ R_{0,3} R_{0,2} R_{0,1} K_0^- R_{1,0} R_{2,0} R_{3,0}\right\}$$

$$= \text{tr}_0\left\{K_0^+ R_{0,3} R_{0,2} R_{0,1} K_0^- R_{0,1} R_{0,2} R_{0,3}\right\}$$

$$= K_0^+ R_{0,3} R_{0,2} R_{0,1} K_0^- R_{0,1} R_{0,2} R_{0,3}\Big|_y^y$$

$$= K_0^+\Big|_a^y R_{0,3}\Big|_b^a R_{0,2}\Big|_c^b R_{0,1}\Big|_d^c K_0^-\Big|_e^d R_{0,1}\Big|_f^e R_{0,2}\Big|_g^f R_{0,3}\Big|_y^g$$

$$= R_{0,1}\Big|_d^c K_0^-\Big|_e^d R_{0,1}\Big|_f^e \cdot R_{0,2}\Big|_c^b R_{0,2}\Big|_g^f \cdot R_{0,3}\Big|_b^a K_0^+\Big|_a^y R_{0,3}\Big|_y^g \tag{A.3}$$

$$= R_{0,1}\Big|_d^c K_0^-\Big|_e^d R_{0,1}\Big|_f^e \cdot R_{0,2}^{t_0}\Big|_b^c R_{0,2}\Big|_g^f \cdot R_{0,3}^{t_0}\Big|_a^b K_0^{+t_0}\Big|_y^a R_{0,3}^{t_0}\Big|_g^y$$

$$= (R_{0,1} K_0^- R_{0,1})\Big|_f^c \cdot R_{0,2}^{t_0}\Big|_b^c R_{0',2}\Big|_g^f \cdot (R_{0,3}^{t_0} K_0^{+t_0} R_{0,3}^{t_0})\Big|_g^b$$

$$= (R_{0,1} K_0^- R_{0,1})\Big|^{cf} \cdot (R_{0,2}^{t_0} R_{0',2})\Big|_{cf}^{bg} \cdot (R_{0,3}^{t_0} K_0^{+t_0} R_{0,3}^{t_0})\Big|_{bg}$$

$$= W_1 \cdot W_2 \cdot W_3.$$

In this way, each tensor in Fig. 5 can be explicitly written out:

$$W_1 = \begin{pmatrix} (p+u)a_1a_1 + (p-u)b_1c_1 \\ (p+u)a_1b_1 + (p-u)b_1d_1 \\ (p+u)c_1a_1 + (p-u)d_1c_1 \\ (p+u)c_1b_1 + (p-u)d_1d_1 \end{pmatrix}^t, \tag{A.4}$$

$$W_j = \begin{pmatrix} a_ja_j & a_jb_j & c_ja_j & c_jb_j \\ a_jc_j & a_jd_j & c_jc_j & c_jd_j \\ b_ja_j & b_jb_j & d_ja_j & d_jb_j \\ b_jc_j & b_jd_j & d_jc_j & d_jd_j \end{pmatrix}, \tag{A.5}$$

$$W_N = \begin{pmatrix} (q+u+\eta)a_Na_N + \xi(u+\eta)(a_Nb_N + c_Na_N) + (q-u-\eta)c_Nb_N \\ (q+u+\eta)a_Nc_N + \xi(u+\eta)(a_Nd_N + c_Nc_N) + (q-u-\eta)c_Nd_N \\ (q+u+\eta)b_Na_N + \xi(u+\eta)(b_Nb_N + d_Na_N) + (q-u-\eta)d_Nb_N \\ (q+u+\eta)b_Nc_N + \xi(u+\eta)(b_Nd_N + d_Nc_N) + (q-u-\eta)d_Nd_N \end{pmatrix}. \tag{A.6}$$

Notation. Let $X_{0,j}$ be a linear operator on $\mathcal{H}_0 \otimes \mathcal{H}_j$, and $\{|\alpha\rangle_0\}$ a fixed basis of $\mathcal{H}_0$. Its matrix element with respect to the 0-th space is defined as

$$X_{0,j}\Big|_\beta^\alpha := (\langle\alpha|_0 \otimes \mathbb{I}_j) X_{0,j} (|\beta\rangle_0 \otimes \mathbb{I}_j), \tag{A.7}$$

which is an operator on $\mathcal{H}_j$.

For two operators $X_{0,j}$ and $Y_{0,k}$, the component of their tensor product is defined by

$$(X_{0,j} Y_{0,k})\Big|_{\beta\delta}^{\alpha\gamma} := X_{0,j}\Big|_\beta^\alpha Y_{0,k}\Big|_\delta^\gamma, \tag{A.8}$$

where $\alpha\gamma$ and $\beta\delta$ denote ordered pairs of basis indices.

In the derivation above, repeated upper-lower index pairs are implicitly summed. When composite labels such as $\alpha\gamma$ appear, the summation convention is applied to each component index separately.

The transpose in the 0-th space is defined directly at the level of matrix elements by

$$X_{0,j}^{t_0}\big|_\beta^\alpha := (\langle\beta|_0 \otimes \mathbb{I}_j)\, X_{0,j}\, (|\alpha\rangle_0 \otimes \mathbb{I}_j) = X_{0,j}\big|_\alpha^\beta. \tag{A.9}$$

B   Corollary of the Maximum Modulus Principle

Let $f(z)$ be analytic on the closed disk $|z| \leq R$. Suppose there exists a constant $a > 0$ such that

$$|f(z)| \geq a \quad \text{for all } |z| = R, \tag{B.1}$$

and

$$|f(0)| < a. \tag{B.2}$$

Then $f(z)$ must have at least one zero inside the open disk $|z| < R$.

Assume to the contrary that $f(z)$ has no zeros in the interior of the disk. Since $f(z)$ is analytic and nonzero on $|z| \leq R$, the reciprocal function

$$\varphi(z) = \frac{1}{f(z)} \tag{B.3}$$

is also analytic on the closed disk.

By the assumption, we have

$$|\varphi(0)| = \left|\frac{1}{f(0)}\right| > \frac{1}{a}, \tag{B.4}$$

and on the boundary,

$$|\varphi(z)| = \left|\frac{1}{f(z)}\right| \leq \frac{1}{a} \quad \text{for all } |z| = R. \tag{B.5}$$

This implies that $|\varphi(z)|$ attains a strict maximum at an interior point $z = 0$, namely

$$|\varphi(z)| \leq \frac{1}{a} < |\varphi(0)|, \quad \text{for all } |z| = R. \tag{B.6}$$

This contradicts the maximum modulus principle, which states that the maximum of $|\varphi(z)|$ on a closed domain is achieved on the boundary unless $\varphi(z)$ is constant.

Therefore, the assumption must be false, and $f(z)$ has at least one zero in $|z| < R$.

C Argument Principle: Validation Data

This appendix presents the numerical verification of all detected zero roots via the argument principle. For each candidate, a closed loop composed of five evaluation points as shown in Fig. 9 is used to compute the total argument change of the function $\Lambda(u)$. The chosen offset δ ensures that only one zero is enclosed per loop, and the result $\Delta = 1$ confirms the presence of a zero.

Table C.1: Validation of candidate zero roots for the ground state based on the argument principle. The model parameters are $N = 100$, $p = -0.6$, $q = -0.3$, $\xi = 1.2$, and $\eta = 1$. Each row corresponds to one candidate surrounded by a closed path with offset δ. The columns $\arg_1$-$\arg_5$ list the phase-unwrapped argument values at the five evaluation points. $\Delta = \frac{1}{2\pi}\Delta_C \arg f(z)$ represents the total argument change along the loop.

Index	Real(z_j)	Imag(z_j)	δ	$\arg_1$	$\arg_2$	$\arg_3$	$\arg_4$	$\arg_5$	Δ
1	-1.537797484405	0.000000000000	10^{-12}	-1.57	-0.00	1.57	3.14	4.71	1.0
2	-1.499950624342	0.010265201348	10^{-12}	-0.32	1.25	2.82	4.39	5.96	1.0
3	-1.499950624342	-0.010265201348	10^{-12}	-2.82	-1.25	0.32	1.89	3.46	1.0
4	-1.499826137427	0.020485525878	10^{-12}	2.47	4.04	5.61	7.18	8.75	1.0
5	-1.499826137427	-0.020485525878	10^{-12}	0.67	2.24	3.81	5.38	6.95	1.0
6	-1.499668437249	0.030659439714	10^{-12}	-1.05	0.52	2.09	3.66	5.23	1.0
7	-1.499668437249	-0.030659439714	10^{-12}	-2.09	-0.52	1.05	2.62	4.19	1.0
8	-1.499508982879	0.040805650649	10^{-12}	1.69	3.26	4.83	6.40	7.97	1.0
9	-1.499508982879	-0.040805650649	10^{-12}	1.45	3.03	4.60	6.17	7.74	1.0
10	-1.499362827910	0.050950483670	10^{-12}	-1.88	-0.31	1.26	2.83	4.40	1.0
11	-1.499362827910	-0.050950483670	10^{-12}	-1.26	0.31	1.88	3.45	5.03	1.0
12	-1.499234729326	0.061118328765	10^{-12}	2.33	3.90	5.47	7.04	8.61	1.0
13	-1.499234729326	-0.061118328765	10^{-12}	0.81	2.38	3.95	5.52	7.09	1.0
14	-1.499124661078	0.071329849178	10^{-12}	-0.35	1.22	2.79	4.36	5.93	1.0
15	-1.499124661078	-0.071329849178	10^{-12}	-2.79	-1.22	0.35	1.92	3.49	1.0
16	-1.499030724545	0.081602732169	10^{-12}	-3.02	-1.45	0.13	1.70	3.27	1.0
17	-1.499030724545	-0.081602732169	10^{-12}	-0.13	1.45	3.02	4.59	6.16	1.0
18	-1.498950502407	0.091952693540	10^{-12}	0.61	2.18	3.75	5.32	6.89	1.0
19	-1.498950502407	-0.091952693540	10^{-12}	2.53	4.10	5.67	7.24	8.81	1.0

Index	Real(z_j)	Imag(z_j)	δ	arg$_1$	arg$_2$	arg$_3$	arg$_4$	arg$_5$	Δ
20	-1.498881624162	0.102394318961	10^{-12}	-2.03	-0.46	1.11	2.68	4.25	1.0
21	-1.498881624162	-0.102394318961	10^{-12}	-1.11	0.46	2.03	3.61	5.18	1.0
22	-1.498821967495	0.112941674848	10^{-12}	1.53	3.10	4.67	6.24	7.81	1.0
23	-1.498821967495	-0.112941674848	10^{-12}	1.61	3.18	4.75	6.32	7.90	1.0
24	-1.498769723486	0.123608744783	10^{-12}	-2.13	-0.56	1.01	2.59	4.16	1.0
25	-1.498769723486	-0.123608744783	10^{-12}	-1.01	0.56	2.13	3.70	5.27	1.0
26	-1.498723364861	0.134409764676	10^{-12}	0.49	2.06	3.63	5.20	6.77	1.0
27	-1.498723364861	-0.134409764676	10^{-12}	2.65	4.22	5.79	7.36	8.94	1.0
28	-1.498681620170	-0.145359467945	10^{-12}	0.04	1.62	3.19	4.76	6.33	1.0
29	-1.498681620170	0.145359467945	10^{-12}	3.10	4.67	6.24	7.81	9.38	1.0
30	-1.498643427402	-0.156473301820	10^{-12}	-2.55	-0.98	0.59	2.16	3.73	1.0
31	-1.498643427402	0.156473301820	10^{-12}	-0.59	0.98	2.55	4.12	5.69	1.0
32	-1.498607890702	-0.167767617858	10^{-12}	1.14	2.71	4.28	5.86	7.43	1.0
33	-1.498607890702	0.167767617858	10^{-12}	2.00	3.57	5.14	6.71	8.28	1.0
34	-1.498574252042	-0.179259858798	10^{-12}	-1.71	-0.14	1.43	3.00	4.58	1.0
35	-1.498574252042	0.179259858798	10^{-12}	-1.43	0.14	1.71	3.28	4.85	1.0
36	-1.498541855015	-0.190968750517	10^{-12}	2.28	3.86	5.43	7.00	8.57	1.0
37	-1.498541855015	0.190968750517	10^{-12}	0.86	2.43	4.00	5.57	7.14	1.0
38	-1.498510123234	-0.202914506180	10^{-12}	-2.87	-1.30	0.27	1.84	3.41	1.0
39	-1.498510123234	0.202914506180	10^{-12}	-0.27	1.30	2.87	4.44	6.01	1.0
40	-1.498478538264	-0.215119055622	10^{-12}	-2.81	-1.24	0.33	1.90	3.48	1.0
41	-1.498478538264	0.215119055622	10^{-12}	-0.33	1.24	2.81	4.38	5.95	1.0
42	-1.498446620333	-0.227606305494	10^{-12}	2.19	3.76	5.33	6.90	8.48	1.0
43	-1.498446620333	0.227606305494	10^{-12}	0.95	2.52	4.09	5.66	7.23	1.0
44	-1.498413915387	-0.240402437913	10^{-12}	-1.56	0.01	1.58	3.15	4.72	1.0
45	-1.498413915387	0.240402437913	10^{-12}	-1.58	-0.01	1.56	3.13	4.70	1.0
46	-1.498379979920	0.253536262645	10^{-12}	2.23	3.80	5.37	6.94	8.51	1.0
47	-1.498379979920	-0.253536262645	10^{-12}	0.92	2.49	4.06	5.63	7.20	1.0
48	-1.498344367511	0.267039629271	10^{-12}	-0.25	1.32	2.89	4.46	6.03	1.0

Index	Real(z_j)	Imag(z_j)	δ	arg$_1$	arg$_2$	arg$_3$	arg$_4$	arg$_5$	Δ
49	-1.498344367511	-0.267039629271	10^{-12}	-2.89	-1.32	0.25	1.82	3.39	1.0
50	-1.498306617468	0.280947921906	10^{-12}	-2.71	-1.14	0.43	2.00	3.57	1.0
51	-1.498306617468	-0.280947921906	10^{-12}	-0.43	1.14	2.71	4.28	5.85	1.0
52	-1.498266239594	0.295300650461	10^{-12}	2.01	3.58	5.15	6.72	8.29	1.0
53	-1.498266239594	-0.295300650461	10^{-12}	1.14	2.71	4.28	5.85	7.42	1.0
54	-1.498222698566	-0.310142165508	10^{-12}	-1.86	-0.29	1.28	2.85	4.42	1.0
55	-1.498222698566	0.310142165508	10^{-12}	-1.28	0.29	1.86	3.43	5.00	1.0
56	-1.498175399285	-0.325522534071	10^{-12}	2.61	4.19	5.76	7.33	8.90	1.0
57	-1.498175399285	0.325522534071	10^{-12}	0.53	2.10	3.67	5.24	6.81	1.0
58	-1.498123665480	-0.341498614506	10^{-12}	0.25	1.82	3.39	4.96	6.53	1.0
59	-1.498123665480	0.341498614506	10^{-12}	2.89	4.46	6.03	7.60	9.17	1.0
60	-1.498066714188	0.358135397291	10^{-12}	-1.06	0.51	2.08	3.65	5.22	1.0
61	-1.498066714188	-0.358135397291	10^{-12}	-2.08	-0.51	1.06	2.63	4.20	1.0
62	-1.498003623959	-0.375507684154	10^{-12}	1.24	2.81	4.38	5.95	7.52	1.0
63	-1.498003623959	0.375507684154	10^{-12}	1.90	3.47	5.05	6.62	8.19	1.0
64	-1.497933293140	-0.393702223808	10^{-12}	-0.36	1.21	2.78	4.35	5.93	1.0
65	-1.497933293140	0.393702223808	10^{-12}	-2.78	-1.21	0.36	1.93	3.50	1.0
66	-1.497854383995	-0.412820455349	10^{-12}	-0.56	1.01	2.58	4.15	5.72	1.0
67	-1.497854383926	0.412820455322	10^{-12}	-2.58	-1.01	0.56	2.14	3.71	1.0
68	-1.497765248390	0.432982083595	10^{-12}	1.61	3.18	4.75	6.32	7.89	1.0
69	-1.497765245778	-0.432982082050	10^{-12}	1.53	3.10	4.68	6.25	7.82	1.0
70	-1.497663849835	-0.454329835627	10^{-12}	-2.56	-0.99	0.59	2.16	3.73	1.0
71	-1.497663817867	0.454329812915	10^{-12}	-0.59	0.99	2.56	4.13	5.70	1.0
72	-1.497547476813	0.477035682510	10^{-12}	-0.50	1.07	2.64	4.21	5.79	1.0
73	-1.497547289313	-0.477035535699	10^{-12}	-2.64	-1.07	0.50	2.07	3.64	1.0
74	-1.497413408143	-0.501310359159	10^{-12}	1.65	3.22	4.79	6.36	7.93	1.0
75	-1.497412793089	0.501309849137	10^{-12}	1.49	3.06	4.63	6.20	7.77	1.0
76	-1.497255294626	0.527412667506	10^{-12}	-2.88	-1.31	0.26	1.83	3.40	1.0
77	-1.497254083110	-0.527411625020	10^{-12}	-0.26	1.31	2.88	4.46	6.03	1.0

Index	Real(z_j)	Imag(z_j)	δ	$\arg_1$	$\arg_2$	$\arg_3$	$\arg_4$	$\arg_5$	Δ
78	-1.497070337484	-0.555673660500	10^{-12}	-2.07	-0.50	1.07	2.64	4.21	1.0
79	-1.497068864609	0.555672362108	10^{-12}	-1.07	0.50	2.07	3.64	5.21	1.0
80	-1.496845058431	0.586510751527	10^{-12}	2.51	4.09	5.66	7.23	8.80	1.0
81	-1.496843960123	-0.586509770845	10^{-12}	0.63	2.20	3.77	5.34	6.91	1.0
82	-1.496572258922	-0.620483259367	10^{-12}	2.19	3.76	5.33	6.90	8.47	1.0
83	-1.496571777498	0.620482830425	10^{-12}	0.95	2.52	4.09	5.66	7.23	1.0
84	-1.496231071195	0.658339515148	10^{-12}	-0.44	1.13	2.70	4.27	5.84	1.0
85	-1.496230958626	-0.658339417530	10^{-12}	-2.70	-1.13	0.44	2.02	3.59	1.0
86	-1.495795097477	-0.701132402982	10^{-12}	-1.63	-0.06	1.51	3.08	4.65	1.0
87	-1.495795086062	0.701132393799	10^{-12}	-1.51	0.06	1.63	3.20	4.77	1.0
88	-1.495218118382	0.750399337671	10^{-12}	-0.60	0.97	2.54	4.11	5.68	1.0
89	-1.495218118079	-0.750399337475	10^{-12}	-2.54	-0.97	0.60	2.17	3.74	1.0
90	-1.494419555125	-0.808519758323	10^{-12}	-3.08	-1.51	0.06	1.63	3.21	1.0
91	-1.494419554811	0.808519758535	10^{-12}	-0.06	1.51	3.08	4.65	6.22	1.0
92	-1.493242561897	0.879467798895	10^{-12}	-3.09	-1.52	0.06	1.63	3.20	1.0
93	-1.493242557769	-0.879467802695	10^{-12}	-0.06	1.52	3.09	4.66	6.23	1.0
94	-1.491336013025	-0.970656104707	10^{-12}	-2.27	-0.70	0.87	2.44	4.01	1.0
95	-1.491335998112	0.970656121093	10^{-12}	-0.87	0.70	2.27	3.84	5.41	1.0
96	-1.487719917574	1.098563225209	10^{-12}	0.01	1.59	3.16	4.73	6.30	1.0
97	-1.487719897134	-1.098563251194	10^{-12}	3.13	4.70	6.27	7.84	9.41	1.0
98	-1.478277809193	-1.314410092648	10^{-12}	-2.59	-1.02	0.55	2.12	3.69	1.0
99	-1.478277799023	1.314410108052	10^{-12}	-0.55	1.02	2.59	4.16	5.73	1.0
100	-1.192055320267	0.000000000000	10^{-12}	1.57	3.14	4.71	6.28	7.85	1.0
101	-0.500000001273	2.182890275359	10^{-12}	-3.14	-1.57	-0.00	1.57	3.15	1.0
102	-0.499999998727	-2.182890275359	10^{-12}	-0.00	1.57	3.14	4.71	6.28	1.0
103	0.192055320267	-0.000000000000	10^{-12}	-1.57	-0.00	1.57	3.14	4.71	1.0
104	0.478277799023	-1.314410108052	10^{-12}	2.59	4.16	5.73	7.30	8.87	1.0
105	0.478277809193	1.314410092648	10^{-12}	0.55	2.12	3.69	5.26	6.83	1.0
106	0.487719897134	1.098563251194	10^{-12}	-0.01	1.56	3.13	4.70	6.27	1.0

Index	Real(z_j)	Imag(z_j)	δ	arg$_1$	arg$_2$	arg$_3$	arg$_4$	arg$_5$	Δ
107	0.487719917574	-1.098563225209	10^{-12}	-3.13	-1.56	0.01	1.59	3.16	1.0
108	0.491335998112	-0.970656121093	10^{-12}	2.27	3.84	5.41	6.98	8.55	1.0
109	0.491336013025	0.970656104707	10^{-12}	0.87	2.44	4.01	5.58	7.15	1.0
110	0.493242557769	0.879467802695	10^{-12}	3.09	4.66	6.23	7.80	9.37	1.0
111	0.493242561897	-0.879467798895	10^{-12}	0.06	1.63	3.20	4.77	6.34	1.0
112	0.494419554811	-0.808519758535	10^{-12}	3.08	4.65	6.22	7.79	9.36	1.0
113	0.494419555125	0.808519758323	10^{-12}	0.06	1.63	3.21	4.78	6.35	1.0
114	0.495218118079	0.750399337475	10^{-12}	0.60	2.17	3.74	5.31	6.89	1.0
115	0.495218118382	-0.750399337671	10^{-12}	2.54	4.11	5.68	7.25	8.82	1.0
116	0.495795086062	-0.701132393799	10^{-12}	1.63	3.20	4.77	6.34	7.91	1.0
117	0.495795097477	0.701132402982	10^{-12}	1.51	3.08	4.65	6.23	7.80	1.0
118	0.496230958626	0.658339417530	10^{-12}	0.44	2.02	3.59	5.16	6.73	1.0
119	0.496231071195	-0.658339515148	10^{-12}	2.70	4.27	5.84	7.41	8.98	1.0
120	0.496571777498	-0.620482830425	10^{-12}	-2.19	-0.62	0.95	2.52	4.09	1.0
121	0.496572258922	0.620483259367	10^{-12}	-0.95	0.62	2.19	3.76	5.33	1.0
122	0.496843960123	0.586509770845	10^{-12}	-2.51	-0.94	0.63	2.20	3.77	1.0
123	0.496845058431	-0.586510751527	10^{-12}	-0.63	0.94	2.51	4.09	5.66	1.0
124	0.497068864609	-0.555672362108	10^{-12}	2.07	3.64	5.21	6.78	8.35	1.0
125	0.497070337484	0.555673660500	10^{-12}	1.07	2.64	4.21	5.78	7.36	1.0
126	0.497254083110	0.527411625020	10^{-12}	2.88	4.46	6.03	7.60	9.17	1.0
127	0.497255294626	-0.527412667506	10^{-12}	0.26	1.83	3.40	4.97	6.54	1.0
128	0.497412793089	-0.501309849137	10^{-12}	-1.65	-0.08	1.49	3.06	4.63	1.0
129	0.497413408143	0.501310359159	10^{-12}	-1.49	0.08	1.65	3.22	4.79	1.0
130	0.497547289313	0.477035535699	10^{-12}	0.50	2.07	3.64	5.21	6.78	1.0
131	0.497547476813	-0.477035682510	10^{-12}	2.64	4.21	5.79	7.36	8.93	1.0
132	0.497663817867	-0.454329812915	10^{-12}	2.56	4.13	5.70	7.27	8.84	1.0
133	0.497663849835	0.454329835627	10^{-12}	0.59	2.16	3.73	5.30	6.87	1.0
134	0.497765245778	0.432982082050	10^{-12}	-1.61	-0.04	1.53	3.10	4.68	1.0
135	0.497765248390	-0.432982083595	10^{-12}	-1.53	0.04	1.61	3.18	4.75	1.0

Index	Real(z_j)	Imag(z_j)	δ	$\arg_1$	$\arg_2$	$\arg_3$	$\arg_4$	$\arg_5$	Δ
136	0.497854383926	-0.412820455322	10^{-12}	0.56	2.14	3.71	5.28	6.85	1.0
137	0.497854383995	0.412820455349	10^{-12}	2.58	4.15	5.72	7.29	8.86	1.0
138	0.497933293140	-0.393702223808	10^{-12}	0.36	1.93	3.50	5.07	6.64	1.0
139	0.497933293140	0.393702223808	10^{-12}	2.78	4.35	5.93	7.50	9.07	1.0
140	0.498003623959	-0.375507684154	10^{-12}	-1.24	0.33	1.90	3.47	5.05	1.0
141	0.498003623959	0.375507684154	10^{-12}	-1.90	-0.33	1.24	2.81	4.38	1.0
142	0.498066714188	0.358135397291	10^{-12}	1.06	2.63	4.20	5.77	7.34	1.0
143	0.498066714188	-0.358135397291	10^{-12}	2.08	3.65	5.22	6.79	8.36	1.0
144	0.498123665480	-0.341498614506	10^{-12}	-0.25	1.32	2.89	4.46	6.03	1.0
145	0.498123665480	0.341498614506	10^{-12}	-2.89	-1.32	0.25	1.82	3.39	1.0
146	0.498175399285	-0.325522534071	10^{-12}	-2.61	-1.04	0.53	2.10	3.67	1.0
147	0.498175399285	0.325522534071	10^{-12}	-0.53	1.04	2.61	4.19	5.76	1.0
148	0.498222698566	-0.310142165508	10^{-12}	1.86	3.43	5.00	6.58	8.15	1.0
149	0.498222698566	0.310142165508	10^{-12}	1.28	2.85	4.42	5.99	7.56	1.0
150	0.498266239594	0.295300650461	10^{-12}	-2.01	-0.43	1.14	2.71	4.28	1.0
151	0.498266239594	-0.295300650461	10^{-12}	-1.14	0.43	2.01	3.58	5.15	1.0
152	0.498306617468	0.280947921906	10^{-12}	2.71	4.28	5.85	7.42	8.99	1.0
153	0.498306617468	-0.280947921906	10^{-12}	0.43	2.00	3.57	5.14	6.72	1.0
154	0.498344367511	0.267039629271	10^{-12}	0.25	1.82	3.39	4.96	6.53	1.0
155	0.498344367511	-0.267039629271	10^{-12}	2.89	4.46	6.03	7.60	9.17	1.0
156	0.498379979920	0.253536262645	10^{-12}	-2.23	-0.66	0.92	2.49	4.06	1.0
157	0.498379979920	-0.253536262645	10^{-12}	-0.92	0.66	2.23	3.80	5.37	1.0
158	0.498413915387	-0.240402437913	10^{-12}	1.56	3.13	4.70	6.27	7.85	1.0
159	0.498413915387	0.240402437913	10^{-12}	1.58	3.15	4.72	6.29	7.86	1.0
160	0.498446620333	-0.227606305494	10^{-12}	-2.19	-0.62	0.95	2.52	4.09	1.0
161	0.498446620333	0.227606305494	10^{-12}	-0.95	0.62	2.19	3.76	5.33	1.0
162	0.498478538264	-0.215119055622	10^{-12}	2.81	4.38	5.95	7.52	9.09	1.0
163	0.498478538264	0.215119055622	10^{-12}	0.33	1.90	3.48	5.05	6.62	1.0
164	0.498510123234	-0.202914506180	10^{-12}	2.87	4.44	6.01	7.59	9.16	1.0

Index	Real(z_j)	Imag(z_j)	δ	arg_1	arg_2	arg_3	arg_4	arg_5	Δ
165	0.498510123234	0.202914506180	10^{-12}	0.27	1.84	3.41	4.98	6.55	1.0
166	0.498541855015	-0.190968750517	10^{-12}	-2.28	-0.71	0.86	2.43	4.00	1.0
167	0.498541855015	0.190968750517	10^{-12}	-0.86	0.71	2.28	3.86	5.43	1.0
168	0.498574252042	-0.179259858798	10^{-12}	1.71	3.28	4.85	6.42	7.99	1.0
169	0.498574252042	0.179259858798	10^{-12}	1.43	3.00	4.57	6.15	7.72	1.0
170	0.498607890702	-0.167767617858	10^{-12}	-1.14	0.43	2.00	3.57	5.14	1.0
171	0.498607890702	0.167767617858	10^{-12}	-2.00	-0.43	1.14	2.71	4.28	1.0
172	0.498643427402	-0.156473301820	10^{-12}	2.55	4.12	5.69	7.27	8.84	1.0
173	0.498643427402	0.156473301820	10^{-12}	0.59	2.16	3.73	5.30	6.87	1.0
174	0.498681620170	-0.145359467945	10^{-12}	-0.04	1.53	3.10	4.67	6.24	1.0
175	0.498681620170	0.145359467945	10^{-12}	-3.10	-1.53	0.04	1.62	3.19	1.0
176	0.498723364861	0.134409764676	10^{-12}	-0.49	1.08	2.65	4.22	5.79	1.0
177	0.498723364861	-0.134409764676	10^{-12}	-2.65	-1.08	0.49	2.06	3.63	1.0
178	0.498769723486	0.123608744783	10^{-12}	2.13	3.70	5.27	6.84	8.41	1.0
179	0.498769723486	-0.123608744783	10^{-12}	1.01	2.59	4.16	5.73	7.30	1.0
180	0.498821967495	0.112941674848	10^{-12}	-1.53	0.04	1.61	3.18	4.75	1.0
181	0.498821967495	-0.112941674848	10^{-12}	-1.61	-0.04	1.53	3.10	4.67	1.0
182	0.498881624162	0.102394318961	10^{-12}	2.03	3.61	5.18	6.75	8.32	1.0
183	0.498881624162	-0.102394318961	10^{-12}	1.11	2.68	4.25	5.82	7.39	1.0
184	0.498950502407	0.091952693540	10^{-12}	-0.61	0.96	2.53	4.10	5.67	1.0
185	0.498950502407	-0.091952693540	10^{-12}	-2.53	-0.96	0.61	2.18	3.75	1.0
186	0.499030724545	0.081602732169	10^{-12}	3.02	4.59	6.16	7.73	9.30	1.0
187	0.499030724545	-0.081602732169	10^{-12}	0.13	1.70	3.27	4.84	6.41	1.0
188	0.499124661078	0.071329849178	10^{-12}	0.35	1.92	3.49	5.06	6.63	1.0
189	0.499124661078	-0.071329849178	10^{-12}	2.79	4.36	5.93	7.51	9.08	1.0
190	0.499234729326	0.061118328765	10^{-12}	-2.33	-0.76	0.81	2.38	3.95	1.0
191	0.499234729326	-0.061118328765	10^{-12}	-0.81	0.76	2.33	3.90	5.47	1.0
192	0.499362827910	0.050950483670	10^{-12}	1.88	3.45	5.03	6.60	8.17	1.0
193	0.499362827910	-0.050950483670	10^{-12}	1.26	2.83	4.40	5.97	7.54	1.0

Index	$\mathrm{Real}(z_j)$	$\mathrm{Imag}(z_j)$	δ	$\arg_1$	$\arg_2$	$\arg_3$	$\arg_4$	$\arg_5$	Δ
194	0.499508982879	0.040805650649	10^{-12}	-1.69	-0.12	1.45	3.03	4.60	1.0
195	0.499508982879	-0.040805650649	10^{-12}	-1.45	0.12	1.69	3.26	4.83	1.0
196	0.499668437249	0.030659439714	10^{-12}	1.05	2.62	4.19	5.76	7.33	1.0
197	0.499668437249	-0.030659439714	10^{-12}	2.09	3.66	5.24	6.81	8.38	1.0
198	0.499826137427	0.020485525878	10^{-12}	-2.47	-0.90	0.67	2.24	3.81	1.0
199	0.499826137427	-0.020485525878	10^{-12}	-0.67	0.90	2.47	4.04	5.61	1.0
200	0.499950624342	0.010265201348	10^{-12}	0.32	1.89	3.46	5.04	6.61	1.0
201	0.499950624342	-0.010265201348	10^{-12}	2.82	4.39	5.96	7.53	9.10	1.0
202	0.537797484405	-0.000000000000	10^{-12}	1.57	3.14	4.71	6.28	7.85	1.0

D Complete Numerical Data of Bethe roots

This appendix provides the numerical data of the Bethe roots shown in Fig. 16. Table D.1 lists the values of λ_j obtained via BA-DMRG together with the relative errors

$$\varepsilon_j = \frac{|\Lambda_{\mathrm{DMRG}}(\lambda_j) - \Lambda_{\mathrm{Bethe}}(\lambda_j)|}{|\Lambda_{\mathrm{DMRG}}(\lambda_j)|}. \tag{D.1}$$

For completeness, the table also includes the quantities

$$G(\lambda_j) = -\frac{A(\lambda_j) + C(\lambda_j)}{B(\lambda_j)}, \tag{D.2}$$

which satisfy $G(\lambda_j) = 1$ when the Bethe Ansatz equations hold.

Table D.1: Complete numerical data of the Bethe roots shown in Fig. 16, including their real and imaginary parts, the relative error ε_j (%), and the real and imaginary components of $G(\lambda_j)$ used to verify the BAEs.

Index	$\mathrm{Real}(\lambda_j)$	$\mathrm{Imag}(\lambda_j)$	ε_j (%)	$\mathrm{Real}(G(\lambda_j))$	$\mathrm{Imag}(G(\lambda_j))$
1	-31.144635856053	14.796601696756	0.006703	0.9999748	-0.0000059
2	-31.144630737854	-14.796570116777	0.001968	1.0000081	0.0000019
3	-31.112214344639	18.776717544408	0.005305	0.9999893	-0.0000181
4	-31.112208092554	-18.776685258374	0.002026	0.9999919	-0.0000011
5	-30.919833829768	11.219153118425	0.007759	0.9999949	0.0000292

6	-30.919829495799	-11.219135908266	0.002844	0.9999911	-0.0000068
7	-30.750239856538	-23.257584807187	0.001043	1.0000008	0.0000041
8	-30.750230653453	23.257621705199	0.003974	0.9999887	-0.0000100
9	-30.488209934679	7.977090964447	0.006454	0.9999946	0.0000257
10	-30.488203635869	-7.977067087444	0.004396	1.0000098	-0.0000153
11	-29.948109813107	-28.392450661966	0.001033	0.9999971	0.0000029
12	-29.948102286317	28.392480724581	0.000886	1.0000025	-0.0000021
13	-29.886471861961	5.021871040236	0.003508	1.0000000	0.0000141
14	-29.886461311705	-5.021851430529	0.001440	0.9999936	-0.0000027
15	-29.139854377934	2.324152165557	0.001858	0.9999990	0.0000071
16	-29.139835112891	-2.324131745496	0.001823	1.0000068	-0.0000037
17	-28.554561157903	-0.000001725273	0.006368	0.9999900	-0.0000276
18	-28.520722851190	-34.445572210226	0.001345	1.0000031	-0.0000037
19	-28.520701034008	34.445623815124	0.002793	0.9999940	-0.0000087
20	-26.110751938488	-41.953134235061	0.001460	0.9999950	-0.0000025
21	-26.110708589107	41.953171369743	0.002460	0.9999910	0.0000024
22	-26.048468541799	-0.000022547448	0.001902	1.0000002	-0.0000044
23	-22.447037966967	-0.000009420298	0.000789	0.9999999	0.0000011
24	-21.813839553443	-52.408293188729	0.001029	1.0000031	-0.0000022
25	-21.813772641141	52.408320918356	0.001338	0.9999953	0.0000016
26	-18.842897834547	-0.000007572427	0.000416	1.0000003	-0.0000004
27	-15.230029186526	-0.000004753581	0.000205	1.0000000	0.0000002
28	-11.600089350039	-0.000003342822	0.000114	1.0000000	-0.0000000
29	-7.929151648995	-0.000002102855	0.000109	1.0000000	0.0000000
30	-4.110450929140	-0.000001008757	0.000095	1.0000000	-0.0000000
31	-0.500000277559	2.257510359594	0.000391	1.0000000	0.0000000
32	-0.500000003504	1.129742222110	0.000021	1.0000000	0.0000000
33	-0.500000002047	0.924097200566	0.000011	1.0000000	0.0000000
34	-0.500000001365	0.799746423715	0.000007	1.0000000	0.0000000
35	-0.500000000989	0.710186993779	0.000006	1.0000000	0.0000000
36	-0.500000000754	0.640008902738	0.000005	1.0000000	0.0000000

37	-0.500000000597	0.582172536749	0.000004	1.0000000	0.0000000
38	-0.500000000484	0.532866814709	0.000003	1.0000000	0.0000000
39	-0.500000000401	0.489794157209	0.000003	1.0000000	-0.0000000
40	-0.500000000337	0.451461607346	0.000003	1.0000000	-0.0000000
41	-0.500000000287	0.416843660349	0.000002	1.0000000	0.0000000
42	-0.500000000246	0.385204975890	0.000002	1.0000000	-0.0000000
43	-0.500000000213	0.355999829697	0.000002	1.0000000	0.0000000
44	-0.500000000185	0.328811599828	0.000002	1.0000000	-0.0000000
45	-0.500000000162	0.303314558595	0.000002	1.0000000	0.0000000
46	-0.500000000142	0.279248772918	0.000002	1.0000000	0.0000000
47	-0.500000000125	0.256403055904	0.000002	1.0000000	-0.0000000
48	-0.500000000110	0.234603050708	0.000002	1.0000000	-0.0000000
49	-0.500000000096	0.213702691298	0.000001	1.0000000	0.0000000
50	-0.500000000085	0.193577946499	0.000001	1.0000000	0.0000000
51	-0.500000000074	0.174122144742	0.000001	1.0000000	0.0000000
52	-0.500000000064	0.155242415665	0.000001	1.0000000	-0.0000000
53	-0.500000000055	0.136856934878	0.000001	1.0000000	0.0000000
54	-0.500000000047	0.118892754934	0.000001	1.0000000	0.0000000
55	-0.500000000039	0.101284069415	0.000001	1.0000000	0.0000000
56	-0.500000000032	0.083970799891	0.000001	1.0000000	0.0000000
57	-0.500000000025	0.066897424863	0.000001	1.0000000	-0.0000000
58	-0.500000000019	0.050011990054	0.000001	1.0000000	0.0000000
59	-0.500000000012	0.033265253604	0.000001	1.0000000	-0.0000000
60	-0.500000000006	0.016609929569	0.000001	1.0000000	-0.0000000
61	-0.499999999994	-0.016609929569	0.000001	1.0000000	0.0000000
62	-0.499999999988	-0.033265253604	0.000001	1.0000000	0.0000000
63	-0.499999999981	-0.050011990054	0.000001	1.0000000	-0.0000000
64	-0.499999999975	-0.066897424863	0.000001	1.0000000	0.0000000
65	-0.499999999968	-0.083970799891	0.000001	1.0000000	-0.0000000
66	-0.499999999961	-0.101284069415	0.000001	1.0000000	-0.0000000
67	-0.499999999953	-0.118892754934	0.000001	1.0000000	-0.0000000

68	-0.499999999945	-0.136856934878	0.000001	1.0000000	-0.0000000
69	-0.499999999936	-0.155242415665	0.000001	1.0000000	0.0000000
70	-0.499999999926	-0.174122144742	0.000001	1.0000000	-0.0000000
71	-0.499999999915	-0.193577946499	0.000001	1.0000000	-0.0000000
72	-0.499999999904	-0.213702691298	0.000001	1.0000000	-0.0000000
73	-0.499999999890	-0.234603050708	0.000002	1.0000000	0.0000000
74	-0.499999999875	-0.256403055904	0.000002	1.0000000	0.0000000
75	-0.499999999858	-0.279248772918	0.000002	1.0000000	-0.0000000
76	-0.499999999838	-0.303314558595	0.000002	1.0000000	-0.0000000
77	-0.499999999815	-0.328811599828	0.000002	1.0000000	0.0000000
78	-0.499999999787	-0.355999829697	0.000002	1.0000000	-0.0000000
79	-0.499999999754	-0.385204975890	0.000002	1.0000000	0.0000000
80	-0.499999999713	-0.416843660349	0.000002	1.0000000	-0.0000000
81	-0.499999999663	-0.451461607346	0.000003	1.0000000	0.0000000
82	-0.499999999599	-0.489794157209	0.000003	1.0000000	0.0000000
83	-0.499999999516	-0.532866814709	0.000003	1.0000000	-0.0000000
84	-0.499999999403	-0.582172536749	0.000004	1.0000000	-0.0000000
85	-0.499999999246	-0.640008902738	0.000005	1.0000000	-0.0000000
86	-0.499999999011	-0.710186993779	0.000006	1.0000000	-0.0000000
87	-0.499999998635	-0.799746423715	0.000007	1.0000000	-0.0000000
88	-0.499999997953	-0.924097200566	0.000011	1.0000000	-0.0000000
89	-0.499999996496	-1.129742222110	0.000021	1.0000000	-0.0000000
90	-0.499999722441	-2.257510359594	0.000391	1.0000000	-0.0000000
91	3.110450929140	0.000001008757	0.000095	1.0000000	0.0000000
92	6.929151648995	0.000002102855	0.000109	1.0000000	-0.0000000
93	10.600089350039	0.000003342822	0.000114	1.0000000	0.0000000
94	14.230029186526	0.000004753581	0.000205	1.0000000	-0.0000002
95	17.842897834547	0.000007572427	0.000416	0.9999997	0.0000004
96	20.813772641141	-52.408320918356	0.001338	0.9999980	-0.0000026
97	20.813839553443	52.408293188729	0.001029	0.9999993	-0.0000024
98	21.447037966967	0.000009420298	0.000789	1.0000001	-0.0000011

99	25.048468541799	0.000022547448	0.001902	0.9999997	0.0000045
100	25.110708589107	-41.953171369743	0.002460	0.9999971	-0.0000039
101	25.110751938488	41.953134235061	0.001460	0.9999979	0.0000019
102	27.520701034008	-34.445623815124	0.002793	1.0000024	-0.0000037
103	27.520722851190	34.445572210226	0.001345	0.9999991	-0.0000018
104	27.554561157903	0.000001725273	0.006368	1.0000012	0.0000033
105	28.139835112891	2.324131745496	0.001823	0.9999992	-0.0000005
106	28.139854377934	-2.324152165557	0.001858	0.9999993	-0.0000005
107	28.886461311705	5.021851430529	0.001440	1.0000000	0.0000009
108	28.886471861961	-5.021871040236	0.003508	0.9999983	-0.0000006
109	28.948102286317	-28.392480724581	0.000886	1.0000010	0.0000005
110	28.948109813107	28.392450661966	0.001033	1.0000006	0.0000013
111	29.488203635869	7.977067087444	0.004396	0.9999976	-0.0000010
112	29.488209934679	-7.977090964447	0.006454	0.9999965	-0.0000014
113	29.750230653453	-23.257621705199	0.003974	1.0000017	-0.0000038
114	29.750239856538	23.257584807187	0.001043	1.0000011	0.0000001
115	29.919829495799	11.219135908266	0.002844	0.9999989	0.0000015
116	29.919833829768	-11.219153118425	0.007759	0.9999952	-0.0000010
117	30.112208092554	18.776685258374	0.002026	0.9999994	0.0000018
118	30.112214344639	-18.776717544408	0.005305	1.0000035	-0.0000033
119	30.144630737854	14.796570116777	0.001968	1.0000005	-0.0000015
120	30.144635856053	-14.796601696756	0.006703	1.0000006	-0.0000050

E   Crossover Behavior of the Paired-Line Roots

This appendix provides a detailed account of how the Bethe-root structure evolves as the number of paired-line root pairs increases for $p > 0$. To illustrate the emergence and development of paired-line roots, this section presents their evolution from a single pair to three.

First, as the innermost central roots approach the real axis, a pair of new line roots is

(a) Global configuration of Bethe roots **(b)** Enlarged view of the central region
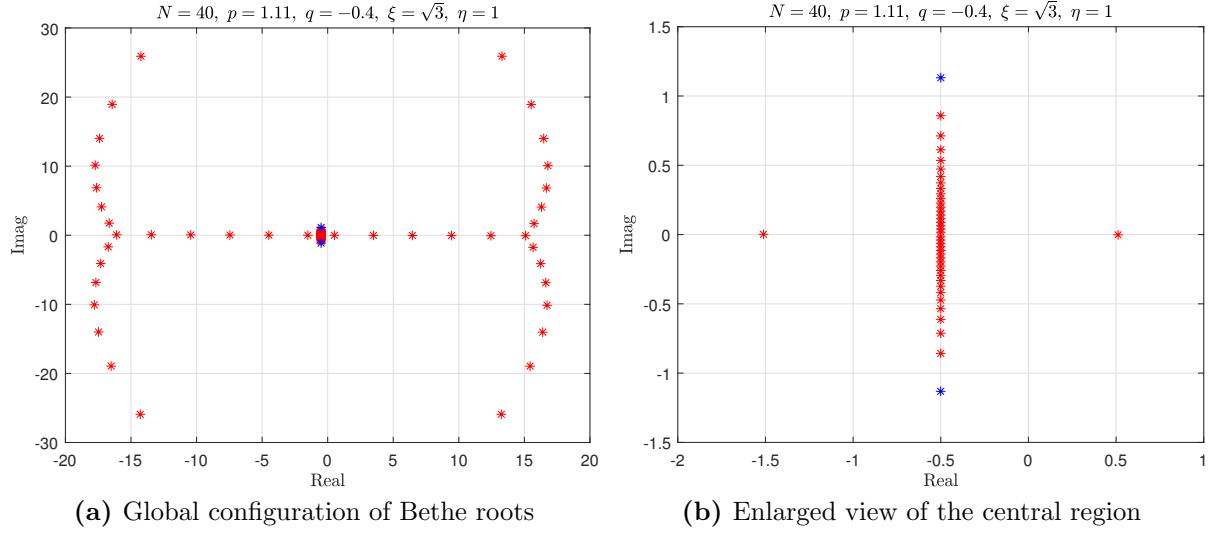
Figure E.1: Distribution of Bethe roots in the complex plane with parameters $N = 40$, $p = 1.11$, $q = -0.4$, $\xi = \sqrt{3}$, and $\eta = 1$. The blue points correspond to the paired-line roots.

generated (Figs. E.1–E.2).

Subsequently, the two new line roots move outward along the real axis, while the outer ones move inward (Fig. E.3).

When the two line roots meet, they coalesce into a paired-line root pair (Fig. E.4)

As evolution proceeds, the two points of the pair continue to separate (Fig. E.5).

However, as the system approaches the next crossover region, the separation between the two points of the paired-line roots contract again (Fig. E.6).

After gradually approaching each other, the two points of the paired-line roots merge and transform back into line roots (Fig. E.7).

In contrast to their initial formation, the two separated points of the line roots move toward each other and eventually meet the adjacent line roots (Fig. E.8).

Upon contact, a new paired-line root pair is formed. Such paired-line root pairs are generated successively outward from the center, indicating that the central paired-line root pair that vanished during the first crossover has reappeared (Fig. E.9).

(a) Global configuration of Bethe roots

(b) Enlarged view of the central region
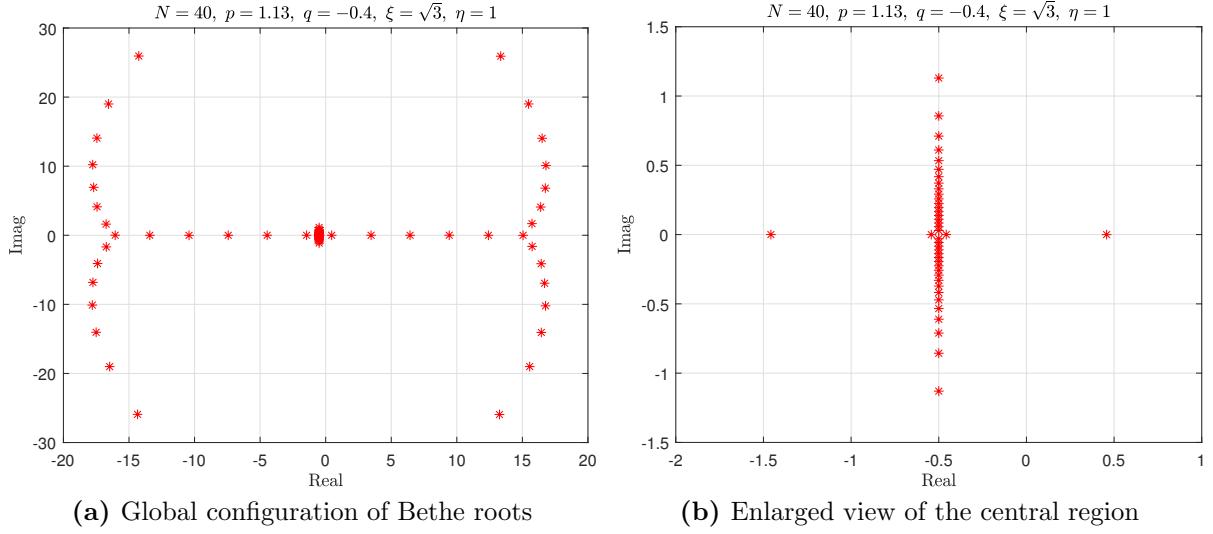
Figure E.2: Distribution of Bethe roots in the complex plane with parameters $N = 40$, $p = 1.13$, $q = -0.4$, $\xi = \sqrt{3}$, and $\eta = 1$.

(a) Global configuration of Bethe roots

(b) Enlarged view of the central region
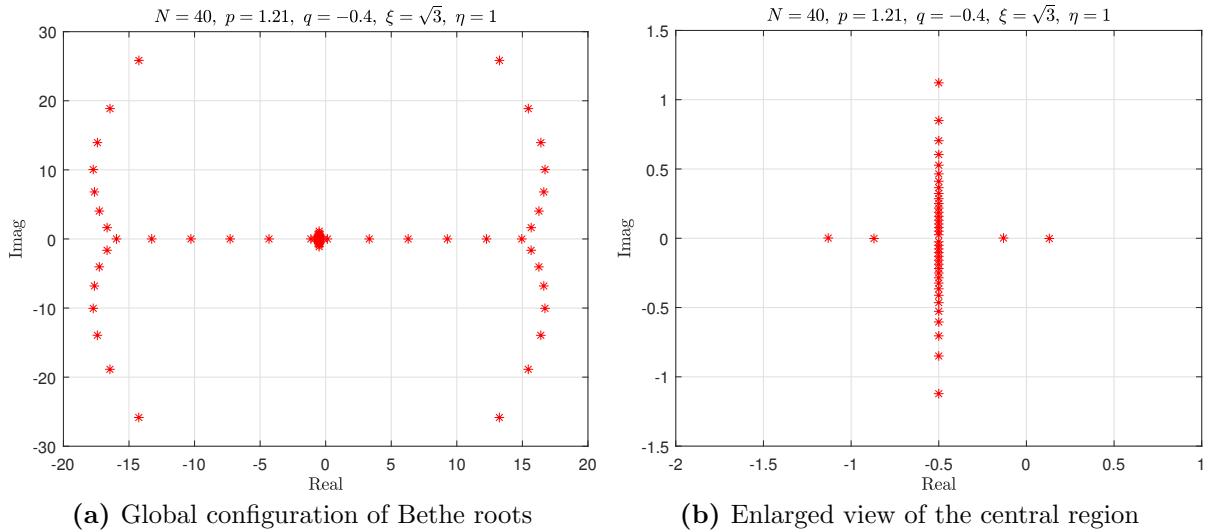
Figure E.3: Distribution of Bethe roots in the complex plane with parameters $N = 40$, $p = 1.21$, $q = -0.4$, $\xi = \sqrt{3}$, and $\eta = 1$.
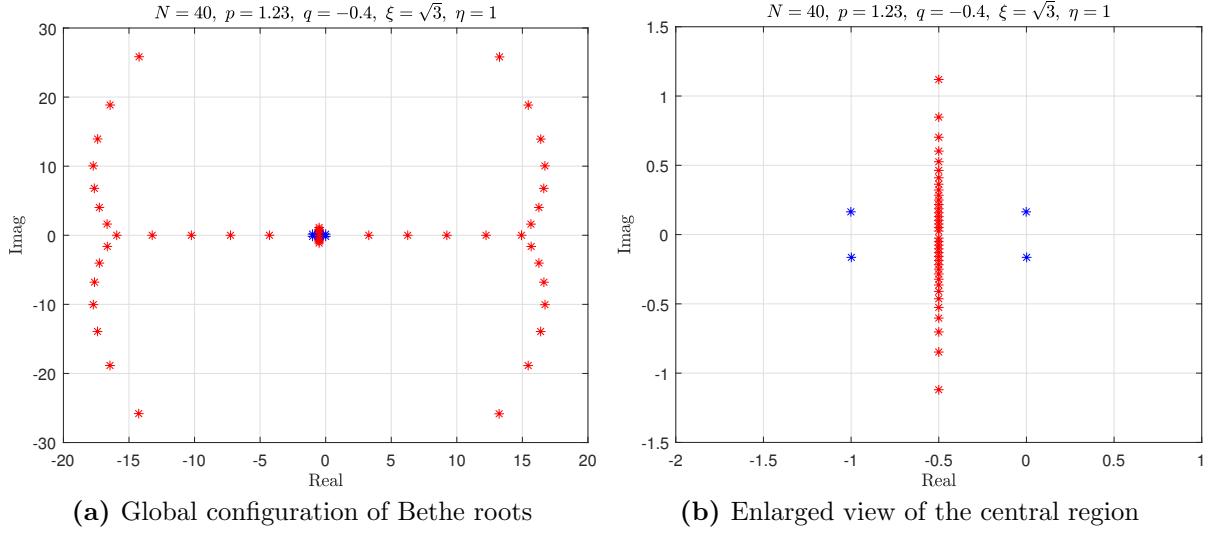
Figure E.4: Distribution of Bethe roots in the complex plane with parameters $N = 40$, $p = 1.23$, $q = -0.4$, $\xi = \sqrt{3}$, and $\eta = 1$. The blue points correspond to the paired-line roots.
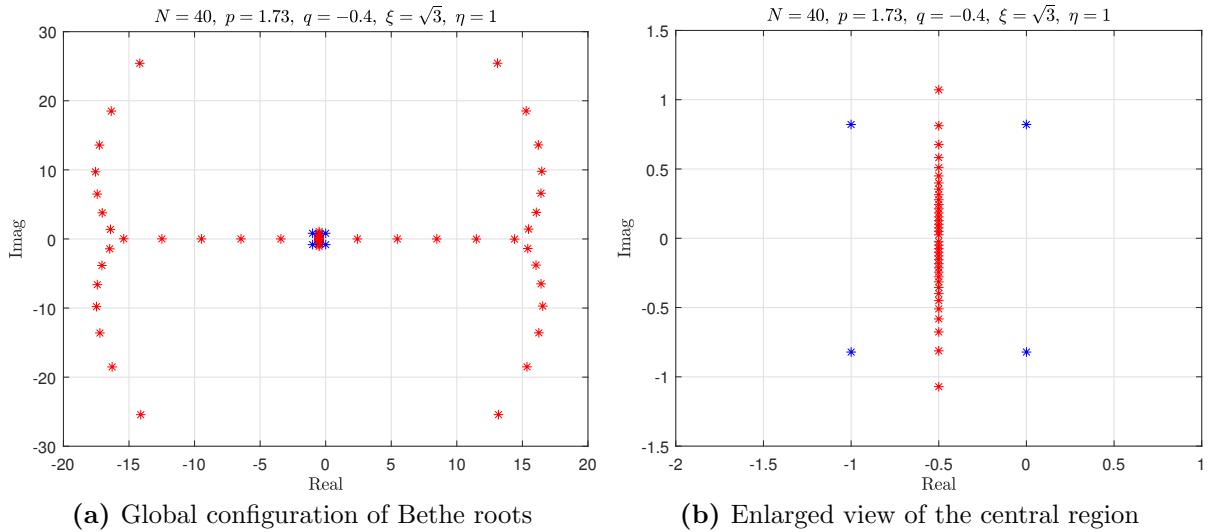
Figure E.5: Distribution of Bethe roots in the complex plane with parameters $N = 40$, $p = 1.73$, $q = -0.4$, $\xi = \sqrt{3}$, and $\eta = 1$. The blue points correspond to the paired-line roots.

(a) Global configuration of Bethe roots

(b) Enlarged view of the central region
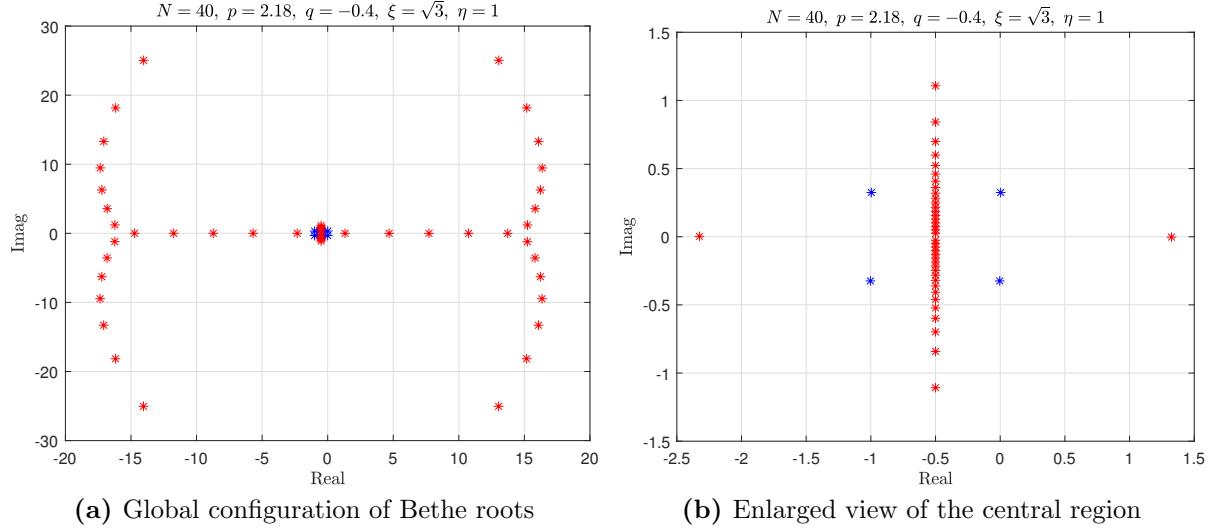
Figure E.6: Distribution of Bethe roots in the complex plane with parameters $N = 40$, $p = 2.18$, $q = -0.4$, $\xi = \sqrt{3}$, and $\eta = 1$. The blue points correspond to the paired-line roots.

(a) Global configuration of Bethe roots

(b) Enlarged view of the central region
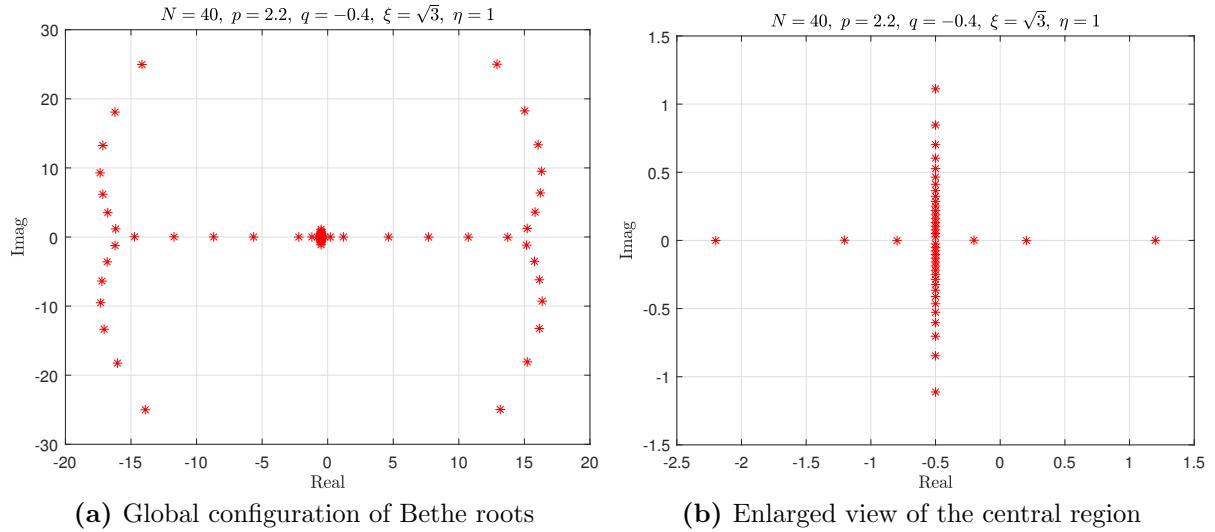
Figure E.7: Distribution of Bethe roots in the complex plane with parameters $N = 40$, $p = 2.2$, $q = -0.4$, $\xi = \sqrt{3}$, and $\eta = 1$.

(a) Global configuration of Bethe roots

(b) Enlarged view of the central region
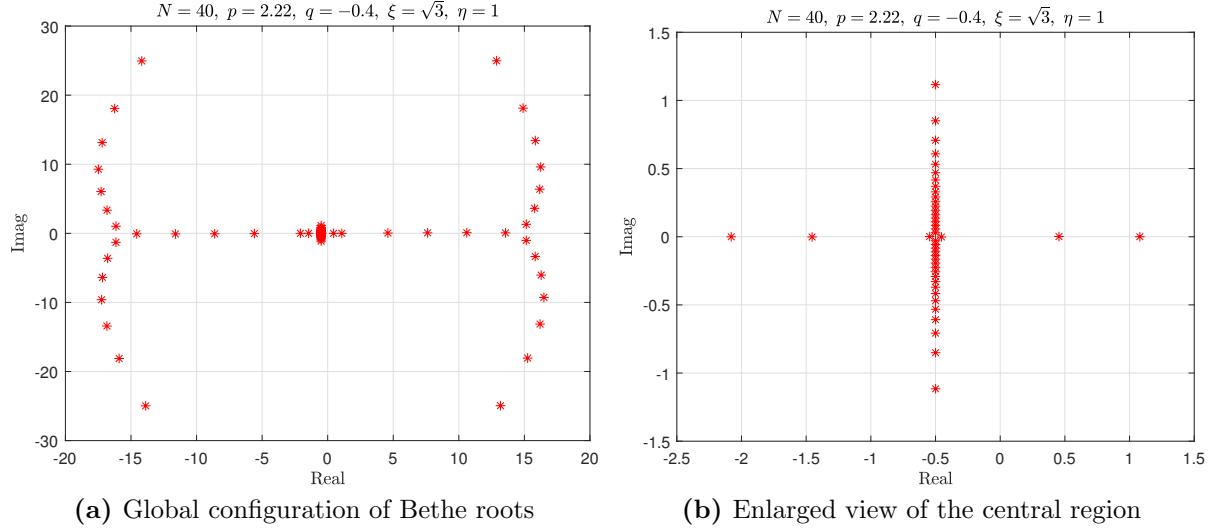
Figure E.8: Distribution of Bethe roots in the complex plane with parameters $N = 40$, $p = 2.22$, $q = -0.4$, $\xi = \sqrt{3}$, and $\eta = 1$.

(a) Global configuration of Bethe roots

(b) Enlarged view of the central region
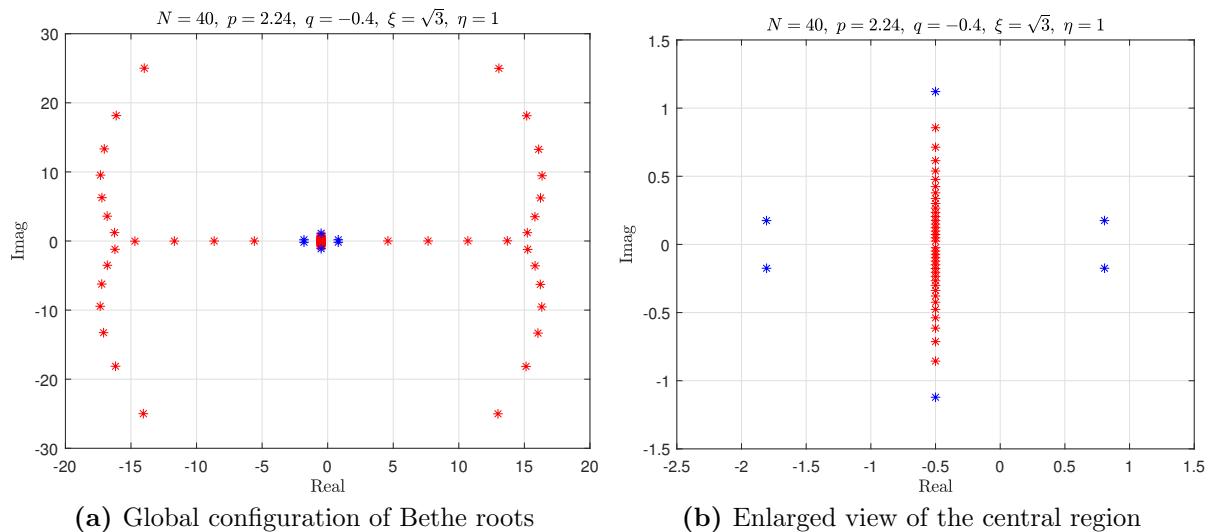
Figure E.9: Distribution of Bethe roots in the complex plane with parameters $N = 40$, $p = 2.24$, $q = -0.4$, $\xi = \sqrt{3}$, and $\eta = 1$. The blue points correspond to the paired-line roots.

References

[1] H. Bethe, Zur Theorie der Metalle, Z. Phys. **71**, 205–226 (1931).

[2] V. E. Korepin, N. M. Bogoliubov, and A. G. Izergin, Quantum Inverse Scattering Method and Correlation Functions, Cambridge Univ. Press (1993).

[3] M. Takahashi, Thermodynamics of One-Dimensional Solvable Models, Cambridge Univ. Press (1999).

[4] R. J. Baxter, Exactly Solved Models in Statistical Mechanics, Academic Press (1982).

[5] L.D. Faddeev, Quantum inverse scattering method. Sov. Sci. Rev. Math. C 1, 107 (1980)

[6] E.K. Sklyanin, L.A. Takhtajan, L.D. Faddeev, Qunatum inverse problem method. Theor. Math. Phys. 40, 688 (1980)

[7] E. K. Sklyanin, Boundary conditions for integrable quantum systems, J. Phys. A **21**, 2375–2390 (1988).

[8] I. V. Cherednik, Factorizing particles on a half line and root systems, Theor. Math. Phys. **61**, 977–983 (1984).

[9] H. J. de Vega and A. Gonzalez Ruiz, Boundary K-matrices for the six vertex and the n(2n-1)A_{n-1} vertex models, J. Phys. A **26**, L519–L524 (1993).

[10] F. C. Alcaraz, M. N. Barber, M. T. Batchelor, R. J. Baxter, and G. R. W. Quispel, Surface exponents of the quantum XXZ, Ashkin-Teller and Potts models, J. Phys. A **20**, 6397–6409 (1987).

[11] L. Mezincescu and R. I. Nepomechie, Integrable open spin chains with nonsymmetric R-matrices, J. Phys. A **24**, L17–L23 (1991).

[12] J. Cao, H. Q. Lin, K. J. Shi and Y. Wang, Exact solution of the XXZ spin chain with unparallel boundary fields, Nucl. Phys. B **663**, 487–519 (2003).

[13] C. M. Yung and M. T. Batchelor, Exact solution of the spin-s XXZ chain with non-diagonal twists, Nucl. Phys. B **446**, 461–484 (1995).

[14] R. I. Nepomechie, Solving the open XXZ spin chain with nondiagonal boundary terms at roots of unity, Nucl. Phys. B **662**, 615 (2002).

[15] P. Baseilhac, The q-deformed analogue of the Onsager algebra: beyond the Bethe ansatz approach, Nucl. Phys. B **754**, 309–345 (2006).

[16] P. Baseilhac and K. Koizumi, Exact spectrum of the XXZ open spin chain from the q-Onsager algebra representation theory, J. Stat. Mech. **2007**, P09006 (2007).

[17] S. Niekamp, T. Wirth and H. Frahm, The XXZ model with anti-periodic twisted boundary conditions, J. Phys. A: Math. Theor. **42**, 195008 (2009).

[18] G. Niccoli, Antiperiodic spin-1/2 XXZ quantum chains by separation of variables: complete spectrum and form factors, Nucl. Phys. B **870**, 397 (2013).

[19] S. Belliard, Modified algebraic Bethe ansatz for XXZ chain on the segment-I: Triangular cases, Nucl. Phys. B **892**, 1 (2015).

[20] S. Belliard and R. A. Pimenta, Modified algebraic Bethe ansatz for XXZ chain on the segment-II-general cases, Nucl. Phys. B **894**, 527 (2015).

[21] J. Cao, W. L. Yang, K. Shi and Y. Wang, Off-diagonal Bethe ansatz and exact solution of a topological spin ring, Phys. Rev. Lett. **111**, 137201 (2013).

[22] Y. Wang, W. L. Yang, J. Cao and K. Shi, *Off-diagonal Bethe Ansatz for Exactly Solvable Models* (Springer, Berlin, 2015).

[23] C. N. Yang and C. P. Yang, Thermodynamics of a one-dimensional system of bosons with repulsive delta-function interaction, J. Math. Phys. **10**, 1115 (1969).

[24] M. Gaudin, Thermodynamics of the Heisenberg-Ising Ring for $\Delta \geq 1$, Phys. Rev. Lett. **26**, 1301 (1971).

[25] M. Takahashi, One-dimensional Heisenberg model at finite temperature, Prog. Theor. Phys. **46**, 401 (1971).

[26] Y. Qiao, P. Sun, J. Cao, W. L. Yang, K. Shi and Y. Wang, Exact ground state and elementary excitations of a topological spin chain, Phys. Rev. B **102**, 085115 (2020).

[27] Y. Qiao, J. Cao, W. L. Yang, K. Shi and Y. Wang, Exact surface energy and helical spinons in the XXZ spin chain with arbitrary nondiagonal boundary fields, Phys. Rev. B **103**, L220401 (2021).

[28] J. Cao, W.-L. Yang, K. Shi, and Y. Wang, Off-diagonal Bethe ansatz solution of the XXX spin chain with arbitrary boundary conditions, Nucl. Phys. B **875**, 152–165 (2013).

[29] R. I. Nepomechie, An inhomogeneous T-Q equation for the open XXX chain with general boundary terms: completeness and arbitrary spin, J. Phys. A **46**, 442002 (2013).

[30] J. Cao, W.-L. Yang, K. Shi, and Y. Wang, Off-diagonal Bethe ansatz solutions of the anisotropic spin-1/2 chains with arbitrary boundary fields, Nucl. Phys. B **877**, 152–175 (2013).

[31] S. R. White, Density matrix formulation for quantum renormalization groups, Phys. Rev. Lett. **69**, 2863–2866 (1992).

[32] U. Schollwck, The density-matrix renormalization group, Rev. Mod. Phys. **77**, 259–315 (2005).

[33] U. Schollwck, The density-matrix renormalization group in the age of matrix product states, Ann. Phys. **326**, 96–192 (2011).

[34] F. Verstraete, D. Porras, and J. I. Cirac, Density matrix renormalization group and periodic boundary conditions: A quantum information perspective, Phys. Rev. Lett. **93**, 227205 (2004).

[35] I. P. McCulloch, From density-matrix renormalization group to matrix product states, J. Stat. Mech. **2007**, P10014 (2007).

[36] F. Pollmann, A. M. Turner, E. Berg, and M. Oshikawa, Entanglement spectrum of a topological phase in one dimension, Phys. Rev. B **81**, 064439 (2010).

[37] V. Murg, V. E. Korepin, and F. Verstraete, Algebraic Bethe ansatz and tensor networks, Phys. Rev. B **86**, 045125 (2012).

[38] M. Fishman, S. R. White, and E. M. Stoudenmire, The ITensor software library for tensor network calculations, SciPost Phys. Codebases **4**, 4 (2022).

[39] L. V. Ahlfors, Complex Analysis, McGraw-Hill (1979).

[40] J.-S. Dong, P. Lu, P. Sun, Y. Qiao, J. Cao, K. Hao, and W.-L. Yang, Exact surface energy and elementary excitations of the XXX spin-1/2 chain with arbitrary non-diagonal boundary fields, Chin. Phys. B **32**, 017501 (2023).

[41] S. Belliard and A. Faribault, Ground state solutions of inhomogeneous Bethe equations, SciPost Phys. **4**, 030 (2018).

[42] T. Xiang, Density Matrix and Tensor Network Renormalization, Cambridge Univ. Press (2023).